INTERIM REPORT

CONTRACT NAS8-20629

A NARROW BEAM, BROAD BANDWIDTH OPTICAL COMMUNICATION SYSTEM

SUBMITTED TO

NASA
GEORGE C. MARSHALL SPACE FLIGHT CENTER
HUNTSVILLE, ALABAMA

PREPARED BY
JOHN R. PRIEBE

15 SEPTEMBER 1969

ITT AEROSPACE 15151 BLEDSOE STREET, SAN FERNANDO, CALIFORNIA

INTERIM REPORT

CONTRACT NAS8-20629

A NARROW BEAM, BROAD BANDWIDTH OPTICAL COMMUNICATION SYSTEM

SUBMITTED TO

NASA

GEORGE C. MARSHALL SPACE FLIGHT CENTER

HUNTSVILLE, ALABAMA

PREPARED BY

JOHN R. PRIEBE

AEROSPACE/OPTICAL DIVISION
DEFENSE-SPACE GROUP
AEROSPACE LABORATORIES
15151 BLEDSOE ST • SAN FERNANDO CALIF 91342
INTERNATIONAL TELEPHONE AND TELEGRAPH CORPORATION

15 September 1969

TABLE OF CONTENTS

TABLE OF CONTENTS (Continued)

LIST OF ILLUSTRATIONS

LIST OF ILLUSTRATIONS (Continued)

FORWARD

This document is an interim report in support of contract NAS8-20629 entitled "A Narrow Beam, Broad Bandwidth Optical Communication System." The program is sponsored by the George C. Marshall Space Flight Center of the National Aeronautics and Space Administration, Huntsville, Alabama. The technical representative for the Government contracting officer is Dr. Joseph L. Randall.

This work was performed by the Aerospace/Optical Division of International Telephone and Telegraph Corporation, San Fernando, California. The principal contributors to the program during the period covered by this report were R.L. Clark, E.R. Marcusen, J.R. Priebe, L.W. Sterritt, J.H. Ward, and D.P. Weaver.

Mr. J.H. Ward is the ITT Aerospace Program Manager responsible for this program.

1.0 INTRODUCTION

This interim report is concerned with the modifications and evaluation of the optical communications system developed under contract NAS8-20629. The system equipment is first briefly reviewed and its operation described. Next the report discusses the modifications which were undertaken to improve and upgrade system performance. These changes were made after extensive testing in the laboratory.

Section 3.0 is concerned with the development of a mathematical model with which to judge system performance. Calculations are made for both ideal and noisy communications channels.

Section 4.0 presents the results of both the laboratory and the field tests. The facilities and the experiment techniques are described. Also pointed out is the need for modifications to some of the digital equipment.

2.0 THE ENGINEERING MODEL

This section reviews the operation of the "Narrow Beam, Broad Bandwidth Optical Communications System," which is described in detail in Reference 1. Also discussed are the major modification and improvements made since the beginning of the 12-month field testing period.

2.1 SYSTEM CONFIGURATION

Detailed diagrams of the two terminals of the engineering model are shown in Figures 2-1 and 2-2. A discussion of the major components of the system is given in the following sections. Since both base and remote stations of the engineering model are really ground stations, it is convenient to describe the system operation functionally, i.e., in terms of the "up-link" and "down-link" rather than in terms of the intended U-2 or satellite equipment and the ground equipment.

2.1.1 Up-Link Equipment

The base terminal transmitter unit shown in Figure 2-1a includes a low power CW helium-neon laser operating at 0.633 microns, KD*P electro-optical modulator, and ancillary telescope optics. These components constitute a laser "beacon" that is amplitude modulated with a 10.7 MHz subcarrier. The subcarrier is in turn frequency modulated with a 20 kHz information bandwidth. The crystal oscillator, audio modulator, and crystal modulator driver in the figure are of completely solid-state construction. The KD*P electro-optical

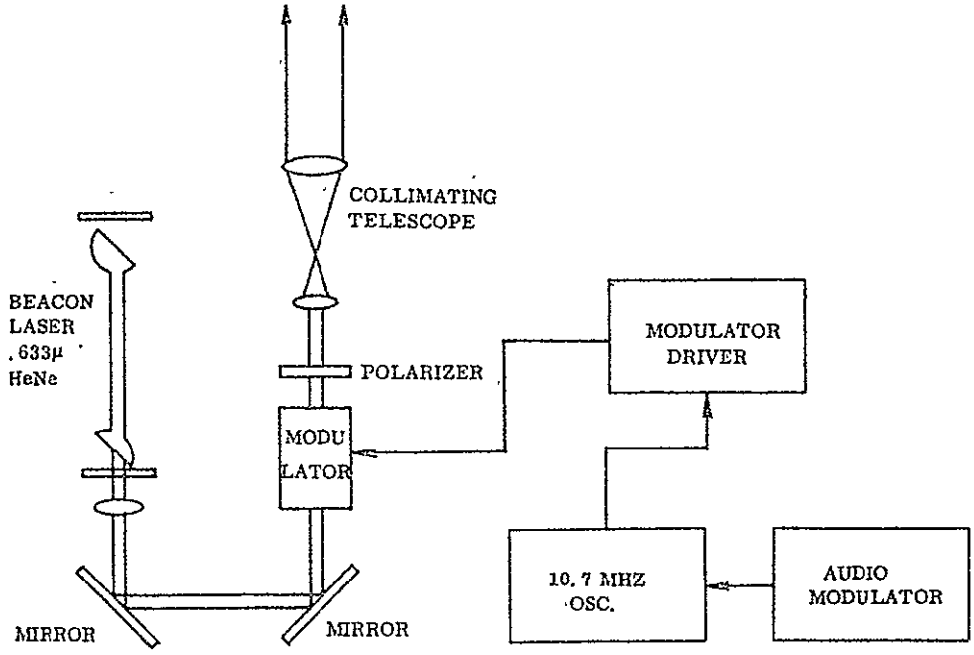

Figure 2-1a. Base Terminal Transmitter Block Diagram.

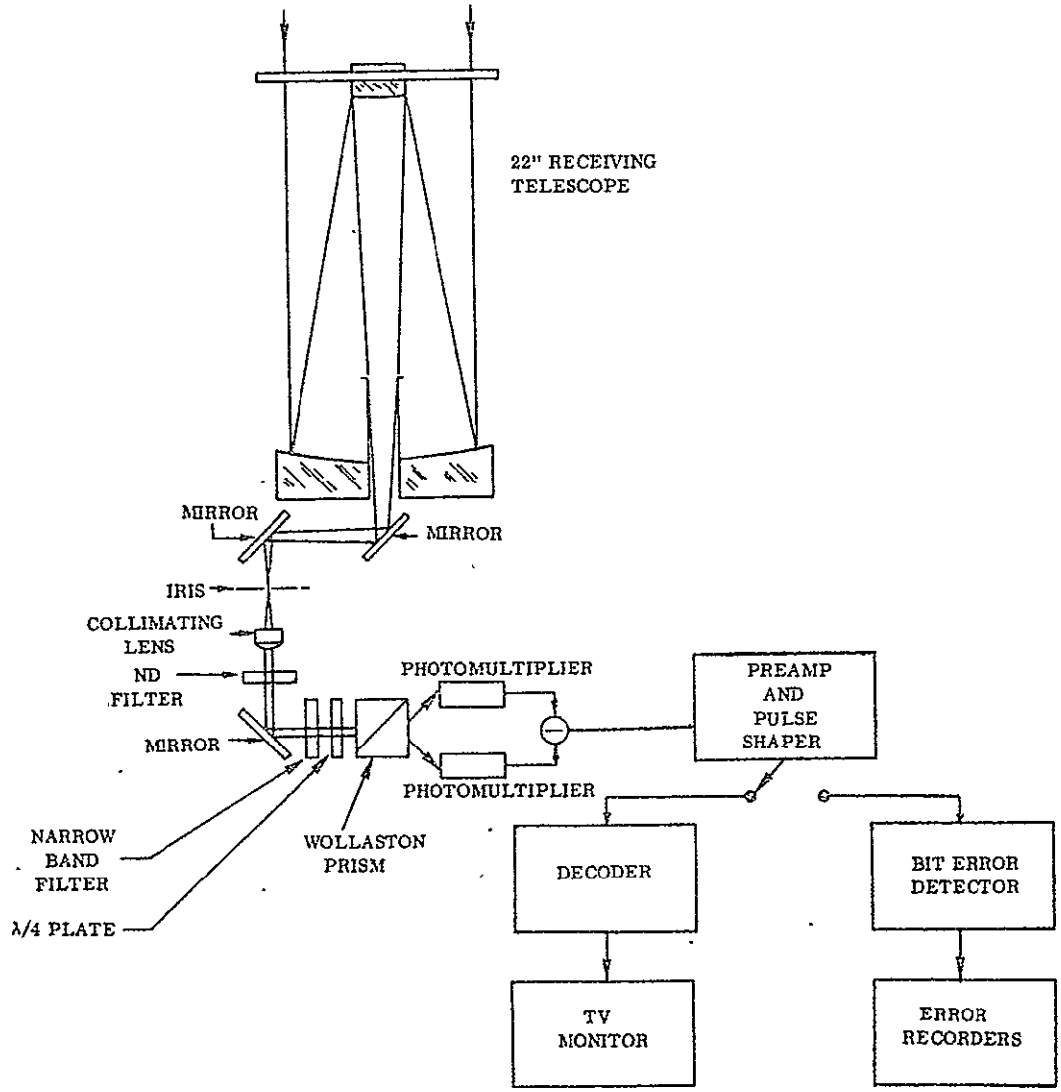

Figure 2-1b. Base Terminal, Receiver Block Diagram.

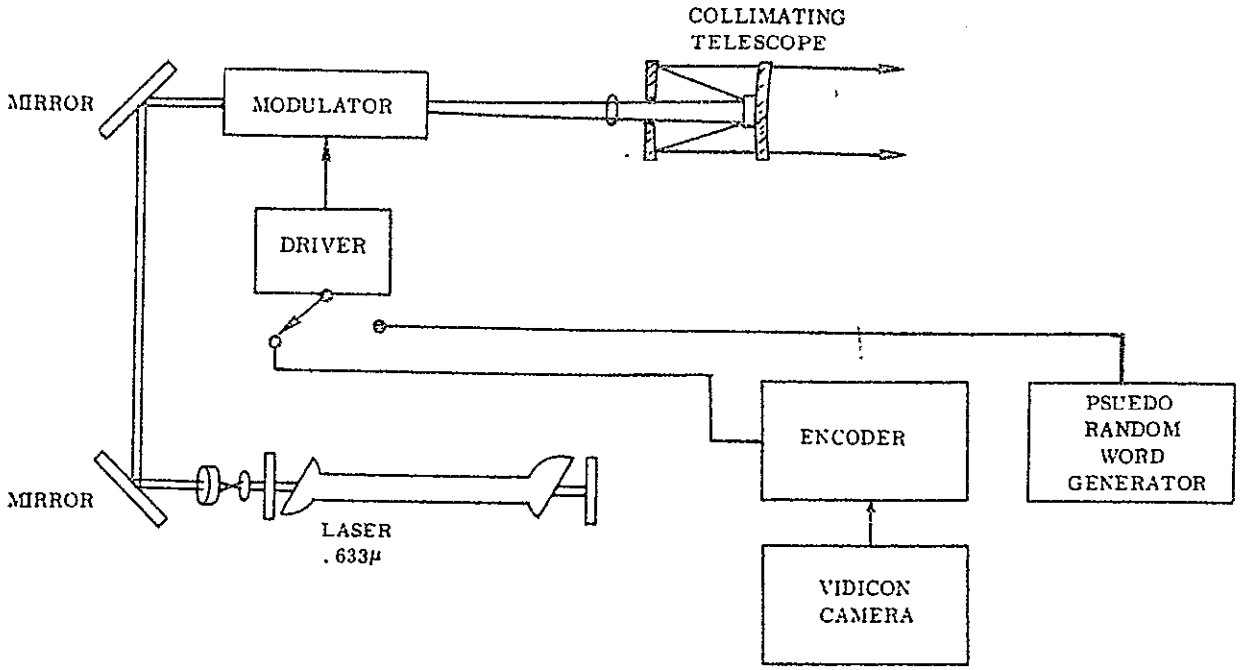

Figure 2-2a. Remote Terminal Block Diagram.

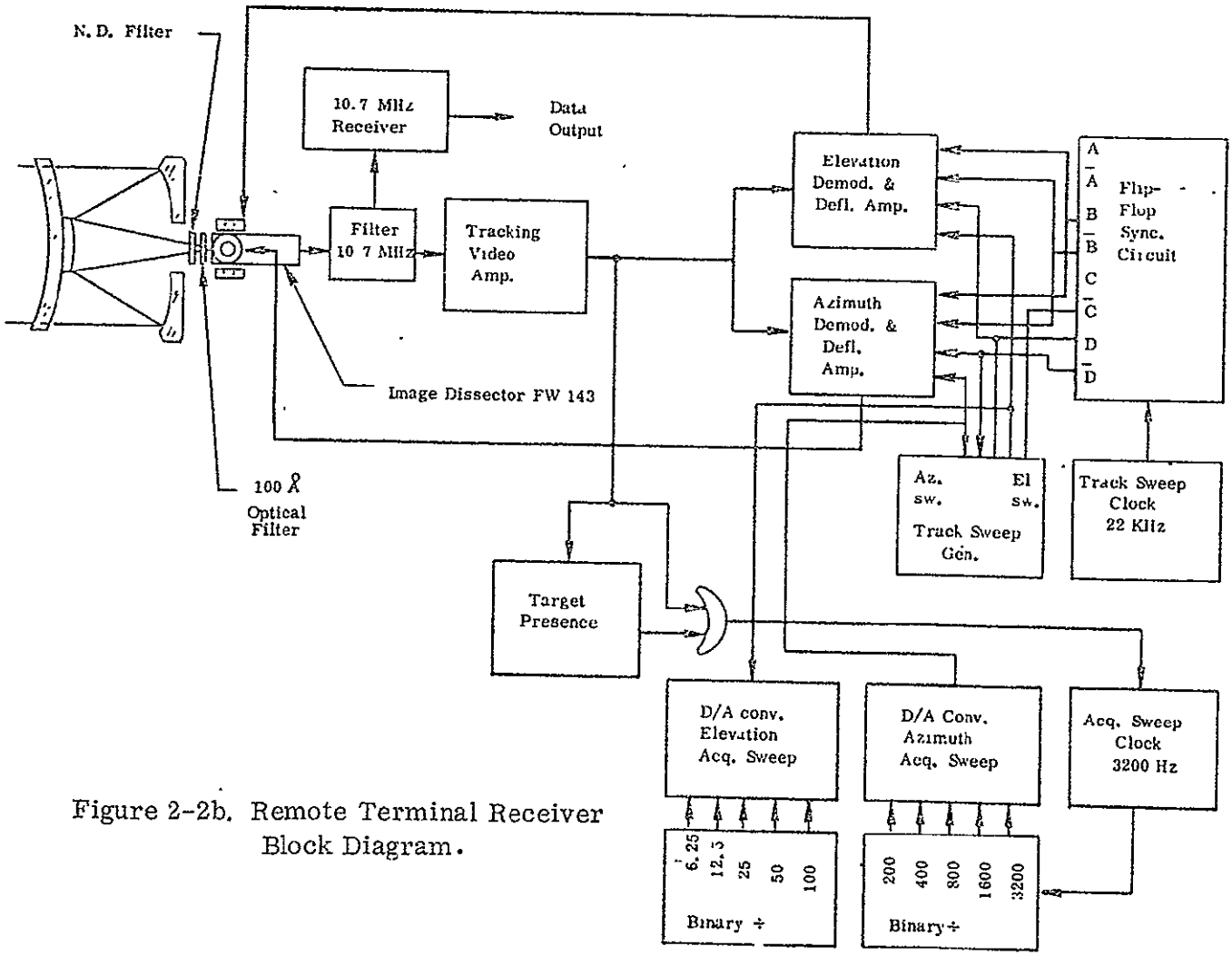

Figure 2-2b. Remote Terminal Receiver Block Diagram.

modulator appears electrically as a 16 pf capacitance, requiring approximately 500 volts rms input for 100 percent modulation of the optical beam. At present, the modulator driver in use is capable of achieving greater than 80 percent modulation of the laser beam.

The modulated laser beacon is collimated by a 60X, 2 inch aperture telescope that is boresighted with the wide bandwidth down-link receiver shown in Figure 2-1b. The collimator for this beacon is adjusted to provide a transmitted beamwidth of about 1 milliradian.

The remote tracking/communicating receiver unit shown in Figure 2-2 includes an f/6.3, 1000 mm focal length collector; ITT image dissector photosensor; and tracking and communicating circuitry. The optical receiver performs the functions of: (a) acquiring the beacon within a 1 degree by 1 degree field-of-view; (b) tracking the beacon position, providing pointing error information relative to the pointing direction of the boresighted down-link transmitter; and (c) detecting the information modulated on the up-link laser beacon.

The tracking/communicating receiver shown in Figure 2-2b uses an image dissector sensor that is capable of electronically scanning its photosensitive surface with a small aperture. This scanning is accomplished by magnetic deflection of the photoelectron beam through a small aperture ahead of the electron multiplier stage.

2.1.2 Down-Link Equipment

The Down-Link Communications System is capable of transmitting either pulse-coded polarization modulation or pulse-coded amplitude modulation on a CW laser beam, both at a 30 megabit data rate. In pulse-coded polarization modulation, the binary ones and zeroes of a message are represented by the state of polarization of the transmitted optical beam. In pulse-coded amplitude modulation, the binary message units are represented by the presence or

absence of the optical carrier. The particular form of modulation depends upon the arrangement of the system's optical components.

A block diagram of the down-link receiver system, operating in a polarization modulation mode, is presented in Figure 2-1b. The linearly polarized output of the down-link CW helium-neon laser is converted into one of two polarization states of an orthogonal set for the 100 percent modulation case. The orthogonal set may consist of either orthogonal linear polarizations, or right-hand and left-hand circular polarizations, depending upon the optical bias on the transmitter's electro-optical modulator. The transmitter unit, shown schematically in Figure 2-2a, consists of the CW laser, transverse field electro-optic modulator, polarization and beam forming optics, and information generating and processing electronics. An industrial quality vidicon camera has been the principal signal source for use in experiments to date. The composite analog signal from the vidicon camera is encoded utilizing a nonreturn-to-zero (NRZ) quantized delta-coding technique.

The source of the remote terminal's optical radiation is a CW helium-neon laser, operating in a single mode (TEM_{00}) at .6328μ, with an output power of approximately 5 mw. The divergence of the laser's output beam is reduced by an inverted telescope, and is subsequently directed through the optical modulator by folding mirrors. If pulsed amplitude (i. e., on-off keying) rather than polarization modulation is desired, a polarization analyzer is placed at the modulator's output, in a crossed orientation with respect to the input plane of polarization. This arrangement allows the transmission of only one intensity varying polarization component.

The down-link modulator is a transverse field KD*P type, with a 20 cm overall crystal length (4 crystals arranged in pairs to cancel natural birefringence) and an optical aperture of 3. 5 mm. The voltage required for $\pi/2$ radian rotation of the transmitted optical electrical field vector is 110 volts. The present all solid-state driver, which supplies a 50 V, 10 nanosecond rise-time pulse across the modulator, achieves a 65 percent modulation depth.

The base terminal receiver unit, shown schematically in Figure 2-1b, includes a 560 mm diameter collection aperture, an adjustable field stop, a 1.5 Å bandpass optical filter, a quarterwave plate, Wollaston prism, photomultiplier detectors, and electronic processing and display equipment. A prism can be inserted into the optical path behind the field stop, to facilitate accurate pointing by sighting through the receiver's optical system. An adjustable field stop permits the receiver's field-of-view to be varied continuously, and provides convenient background control. Neutral density filters can be inserted into the receiver's optical path to produce fixed amounts of optical attenuation. These filters simulate the inverse square geometrical effects of increased range and protect the photodetectors from excessive signal power at shorter ranges. Radiation passing through the field stop is collimated prior to its impinging on the optical filter and quarterwave plate, since performance of these elements is sensitive to a beam's incident angle.

Since there are no phase or polarization sensitive optical detectors, polarization modulation must be converted to an amplitude modulation in the receiver prior to detection. This conversion is accomplished by resolving the incoming polarization state into a set of orthogonal linear components whose amplitudes vary with the incoming polarization state. For the 100 percent modulation condition, the input circular states are converted to an orthogonal linear set by introducing an additional quarterwave bias into the beam. The resulting amplitude varying linear components are then spatially separated and independently detected. Through this split-channel technique, one photodetector receives the binary ones of the message and the other photodetector receives the binary zeroes. The outputs of the two photodetectors are combined in a differential amplifier to reconstruct the originally transmitted pulse train. This pulse train is then decoded in the analog-to-digital converter, and the reconstructed composite video is subsequently displayed on a conventional television monitor.

When amplitude modulation is transmitted, the quarterwave plate and Wollaston prism are removed from the receiver, and only a single detector is used to detect the received beam (single-channel operation).

2.1.3 Bit Error Rate (BER) Measuring Equipment

As will be discussed in Section 3.1.2, the most meaningful assessment of a digital communication system's performance is a measurement of its bit error rate, i.e., the rate at which errors occur between the transmitted and received information. The instrumentation for measuring this quantity is represented by the bit error detector block in Figure 2-1b and the pseudo-random word generator block in Figure 2-2a. These blocks have been expanded in Figure 2-3, and their functions are described next.

A known pseudo-random pulse pattern is generated and synchronized to a local 30 MHz clock in the A/D converter. This pseudo-random word (PSR) is used as the video signal in the 30 MHz transmitter. At the receiver, the detected signal output is coupled to both the bit synchronizer of the D/A converter and the word recognizer. The 30 MHz oscillator in the D/A converter is phase-locked to the incoming bit stream. When the word recognizer detects the proper pattern, it starts a local 32-bit pattern generator, identical to the transmitted word, in phase synchronism with the received signal. The received signal is compared. bit by bit with the output of the local 31-bit pattern generator, in a modulo-2 comparator at the 30 MHz clock rate. The delay on the clock is adjusted so it triggers the output of the modulo-2 comparator at the center of a 33 nanosecond bit period. If the received bit is identical to the transmitted bit, the comparator has no output. When the two signals differ, the clock triggers the output which indicates that an error has occurred in the transmission link. During system evaluation experiments, the output of the bit error detector is both passed to a digital counter and recorded as shown in Figure 4-6.

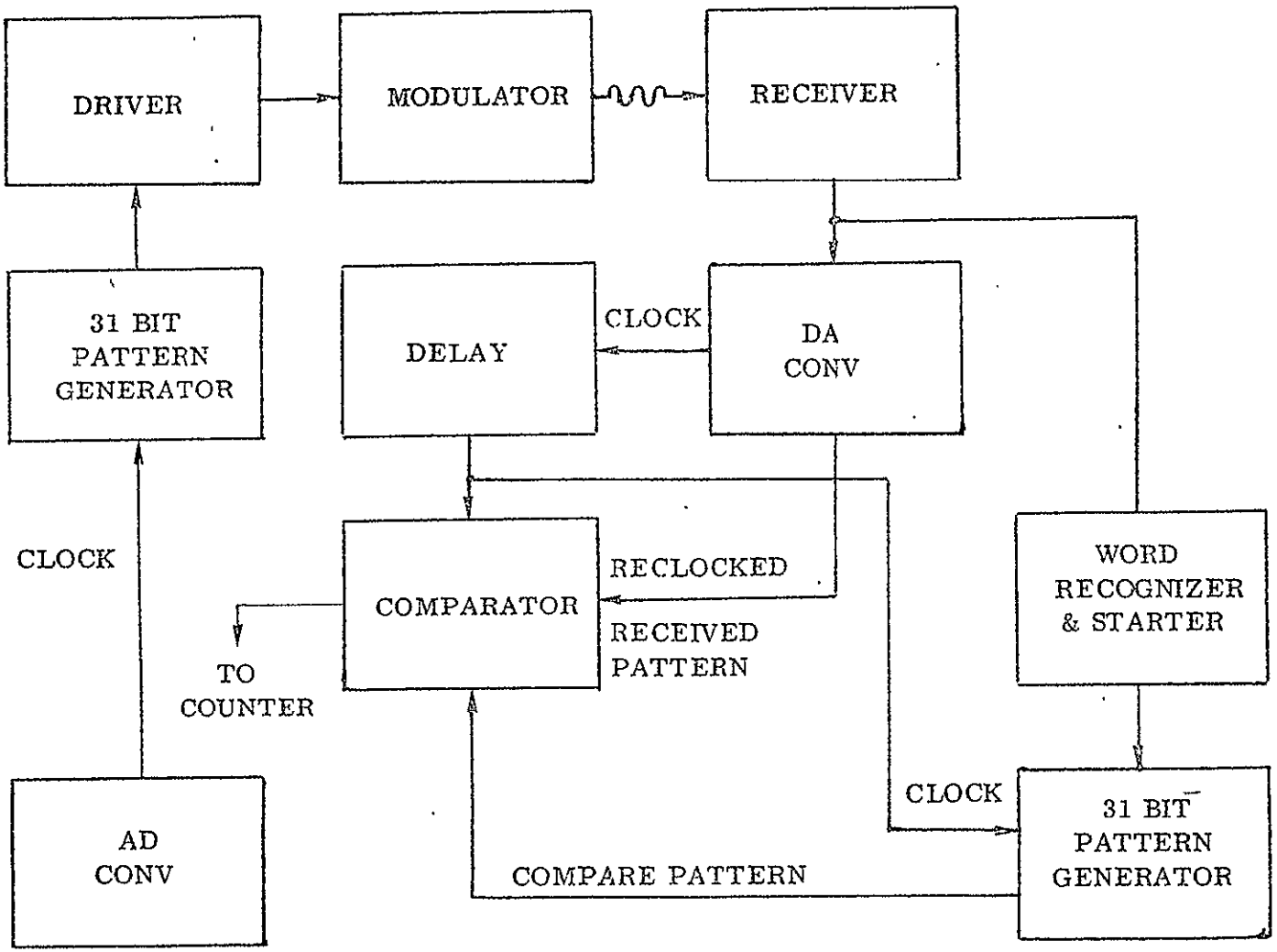

Figure 2-3. Pseudo-Random Word Generator and Bit Error Detector.

2.2 MODIFICATIONS AND IMPROVEMENTS

In the course of testing the optical communications system in the laboratory and field, many opportunities were taken to upgrade the equipment through modifications and additions to various subsystems. This section is concerned with those changes, some of which were funded by ITT.

2.2.1 Installation of New Telescope

The base terminal of the optical link was operated at first with an eight-inch aperture reflecting telescope. System performance with this instrument often proved to be disappointing. Very high radiant signal power levels, resulting in excessively high anode current on the detectors, were frequently required in order to hold the digital equipment in lock. The smoothing advantages of a large optical aperture for the collection of scintillating light are well known, and several theoretical and experimental investigations of "aperture averaging" have been reported. Hence, to improve system performance and also provide a capability for studying the effects of atmospheric turbulence, a larger telescope was acquired. The instrument, a modified 22 inch aperture F/10 Cassegrain, is shown in the Frontispiece.

Operation with this larger aperture yielded a significant improvement in system performance. However during the period that the receiver system was located in the roof-mounted astrodome, there was considerable inconsistency in recorded experimental data. It seemed apparent that the difficulty was due to instability of the telescope's mount. The telescope was mounted atop a 4-foot length of 8-1/2 inch vertical steel tubing. The other end of this tube was attached to an I-beam that is one of the supporting members of the roof. Personnel walking on the roof and other sources of low frequency vibrations in the building caused motion of this I-beam and consequent changes in the telescope's pointing vector. A telescope pointing error of 0.25 milliradians would

translate the received illumination pattern completely across the receiver's instantaneous field-of-view. It was determined that the required order of stability was attainable within the roof-mounted astrodome only with major modifications to the building structure.

For this reason, the base terminal equipment was relocated in a modified mobile trailer. A massive steel tripod, similar to that used in the remote terminal facility, was constructed to support the telescope. This tripod has extendable legs that project through the trailer floor to the earth. Hence, motion in the trailer does not disturb the telescope. This arrangement has alleviated pointing instability problems.

2.2.2 Pulse Shaping and Threshold Circuitry

During laboratory testing of the equipment, a discrepancy was noted between the reported performance of the hardwire and the pseudo-random (PSR) bit error detectors. At low error rates, the hardwire error detector had about one order of magnitude higher error rate. It was also noticed that the delay line that controlled the clock input to the hardwire error detector was difficult to adjust. This delay line was found to be faulty. It had at first been intermittent, and subsequently it failed completely. For this reason, the delay line was returned to the manufacturer for repair. However, after the repaired delay line had been installed, it was found that the PSR error detector exhibited an almost constant order of magnitude higher error rate than the hardwire error detector. This condition was opposite to that noted prior to the delay line's failure.

Investigation of this new phenomena led to the conclusion that the PSR bit error detector was extremely sensitive to pulse width. The received pulse shown in Figure 2-25 of Reference 1 is seen to be narrower than the 33 nanosecond pulse which was applied to the modulator. This was not initially

anticipated as a problem, since the instruction manual for the purchased D/A equipment states that the equipment samples a small slice of the pulse at the clock crossing. In actuality, it requires at least 27 nanoseconds of the 33 nanosecond pulse width to make a valid determination as to the presence or absence of a pulse, while the hardwire bit error detector requires only 11 nanoseconds of the 33 nanosecond pulse width to make the same decision.

To correct this condition with a minimum of modifications, ITT undertook the design of the Pulse Shaping and Thresholding Circuit shown in Figure 2-4. This circuit is a differential amplifier which compares a signal input to a level set by adjusting the 250 ohm potentiometer. With no input signal, Q1 is conducting and Q2 is off. When the input signal level at Q1 exceeds the threshold bias on Q2, the conduction state changes and Q2 conducts. Therefore, a positive input pulse generates a positive output pulse. The variable capacitor at the input is adjusted to change the pulse width seen at the output. This circuit is connected to the receiver preamplifier output in order to condition the received signal for application to the D/A equipment.

After the Pulse Shaping and Threshold circuit was installed in the system, a new error rate comparison was made, and the condition was found to be corrected. At present, the hardwire error detector still operates with its output directly from the receiver preamplifier, while the PSR error detector requires the reconstituted pulse output. For this reason, much can be done to improve the digital portion of this system. An ideal system would only recognize the presence or absence of a pulse during the clock interval, and would remain almost indifferent to pulse width. For example, a pulse differing in width from 11 nanoseconds to 44 nanoseconds, centered about the clock generator crossing, should be recognized as a single pulse. This would allow a 5 nanosecond minimum guardband, but would permit a 4 to 1 variation in pulse width. The present decoding technique allows less than a 2 to 1 variation before contributing errors.

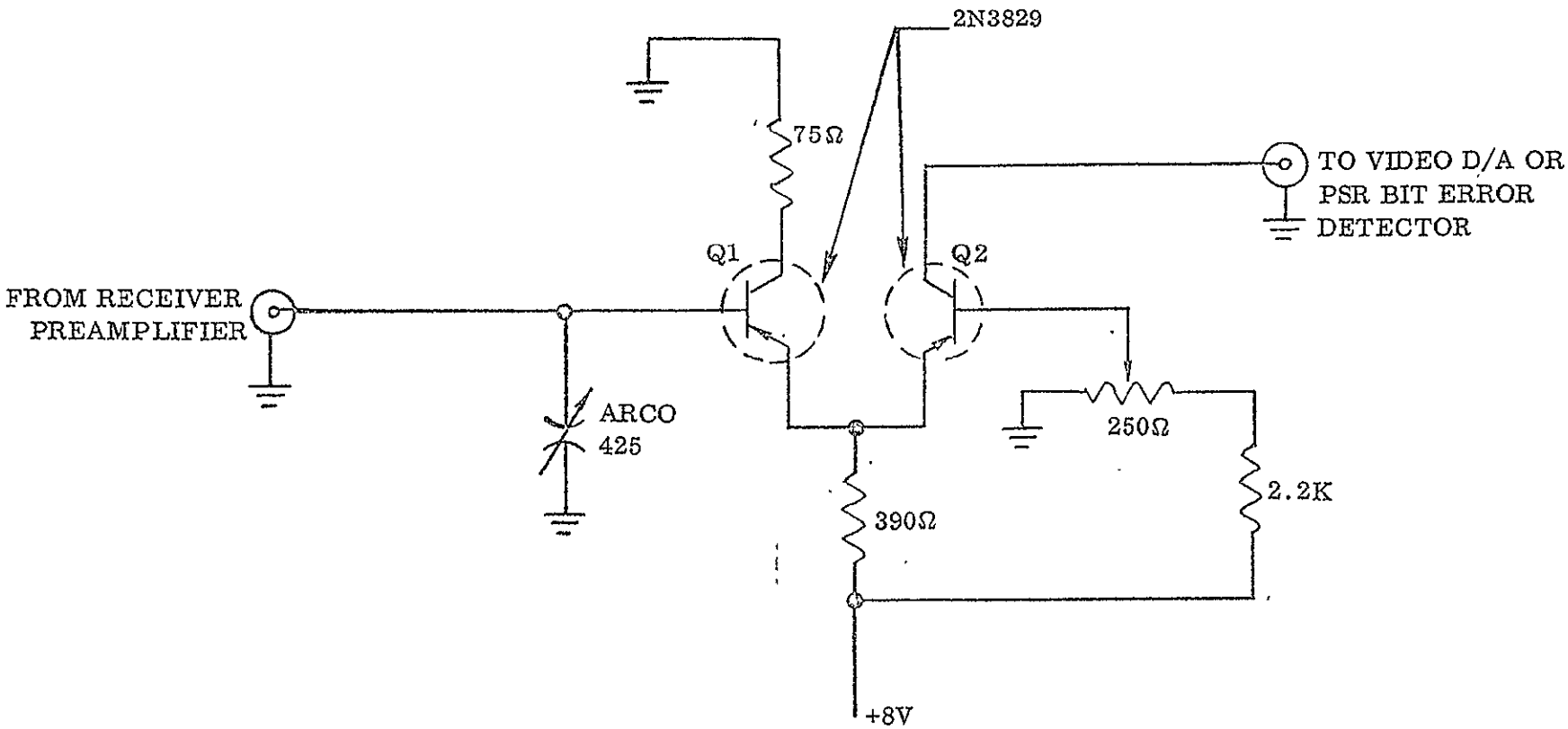

Figure 2-4. Pulse Shaping and Thresholding Circuit.

In Section 2. 5 of Reference 1, analysis indicated that 9 db of gain could be added to the system before reaching the noise threshold of the D/A equipment. By incorporating the Pulse Shaping and Thresholding circuit, 6 db of this gain was added. The effect of this circuit is most noticeable at low modulation depths and low signal levels as shown in Figure 2-5. This is a series of plots of PSR error rate versus modulation depth, for three different signal levels. The plots are made both with and without the Pulse Shaping and Thresholding circuit in order to show the improvement in system performance attributable to this added circuit.

The photographs in Figure 2-6 show the PSR word both with and without the Pulse Shaping and Thresholding circuit. In each photo, the upper trace is the word directly out of the PSR generator. In photograph No. 1, the modulator voltage is 10 volts; the average number of detected photoelectrons per bit, $\overline{N}$, is 440. In the upper portion of the photograph, the preamplifier output in the lower trace is compared with the pseudo-random word generator output. The narrow pulses with noise drop-out are readily observed. In the lower portion of the photograph, the generator output is compared with the output of the Pulse Shaping and Thresholding circuit added to the preamplifier. The similarity in pulse width and decrease in noise drop-outs is evidenced in this PSR word in the lower trace, showing the effectiveness of this circuit. In photograph No. 2, the modulation voltage was 6 volts with an $\overline{N}$ of 440. Again in this picture, the improvement of pulse shaping and thresholding in the lower portion can be observed over that in the upper portion. In photograph No. 3, the modulation voltage was 3 volts and $\overline{N}$ was again 440. The improvements of pulse shaping and thresholding can still be observed in the lower portion of the photograph, over that in the upper portion of the photograph. It can further be observed that we are thresholding near the system noise level, and further improvement must be in the area of reducing system noise prior to adding more gain. This

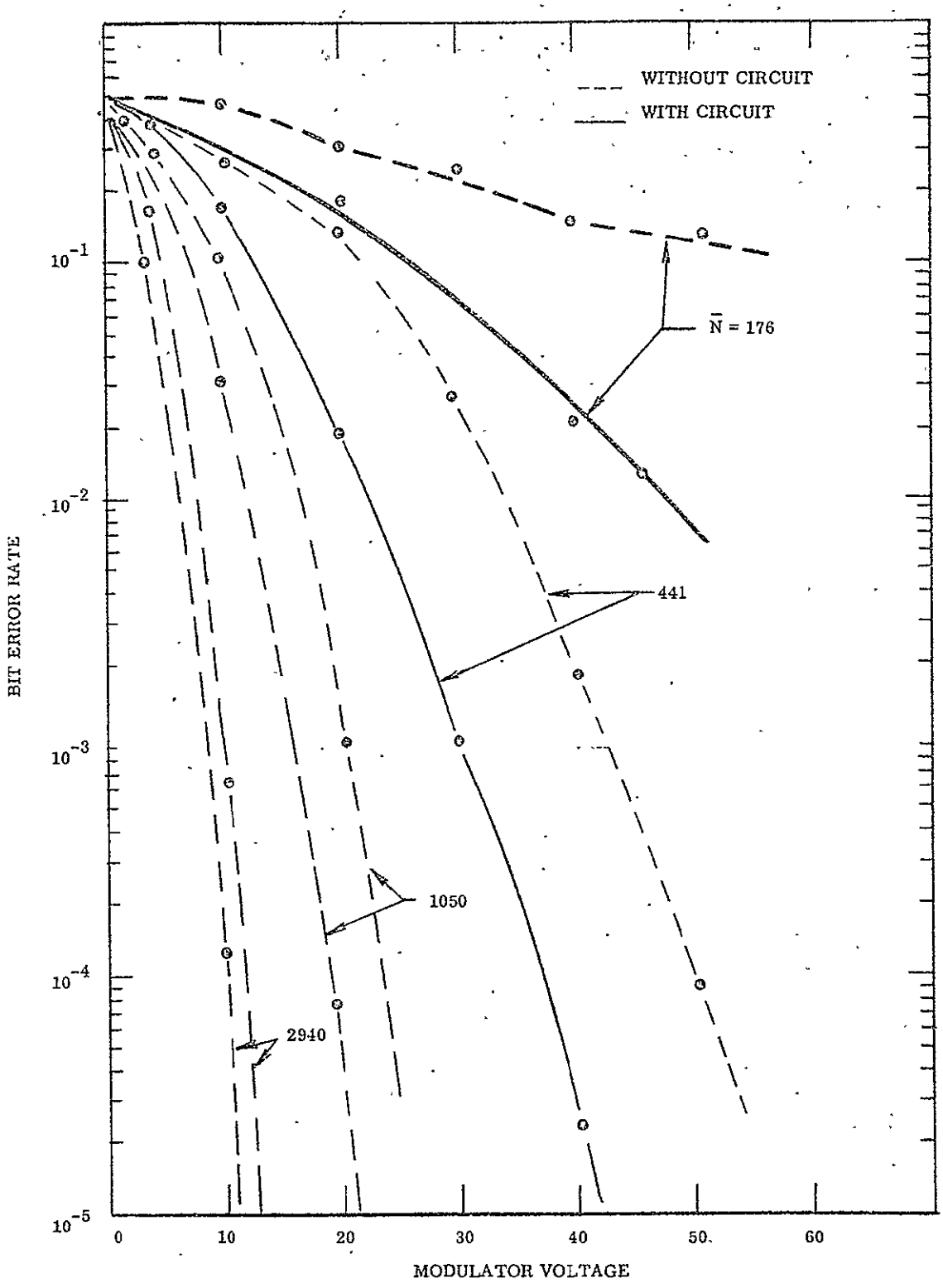

Figure 2-5. Effect of Incorporating Pulse Shaping and Threshold Circuits on the System Bit Error Rate.

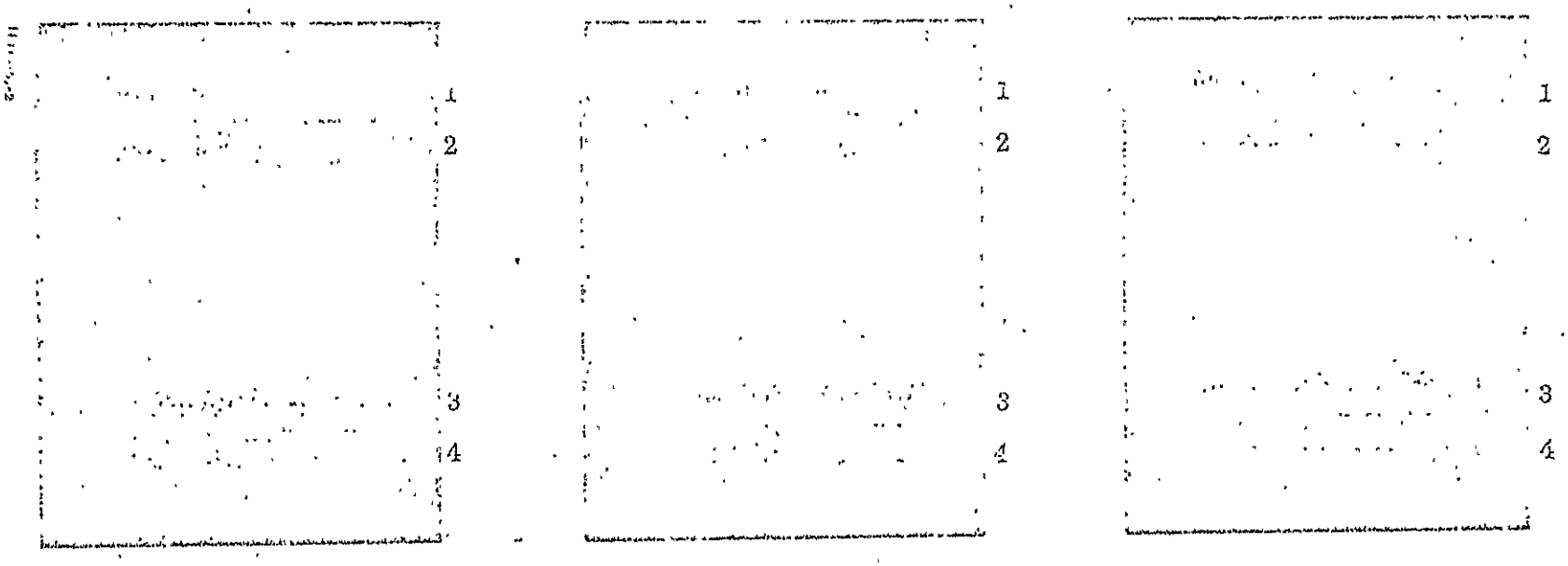

Figure 2-6. Photographs showing the effect of adding Pulse Shaping and Thresholding Circuitry to the Optical receiver. In each photo, traces #1 and #3 are the PSR generator outputs before application to the modulator driver. Trace #2 is the receiver preamplifier output and Trace #4 is the output with the Pulse Shaping network in the circuit.

type of noise is observed rising from the baseline, rather than the drop-out noise observed in photograph No. 1. Such noise is a combination of both shot and thermal noise, since the noise output from the aggregate receiver (comprising the photomultiplier, preamplifier and pulse shaping amplifier) is much less with the laser radiation blocked.

It should be noted that in each photograph, the bit error rate is less with the Pulse Shaping and Thresholding circuit in the system.

2.2.3 Improvements in Instrumentation

At the onset of the field testing program, the quantitative instrumentation consisted of a digital readout counter on the bit error measuring equipment and meters which registered the photomultiplier currents. There were also provisions for connecting other measuring or recording devices to the photomultiplier outputs, but this current loading interfered with the operation of the error measurement. In the incipient measurements, the experimental technique was to record the digital bit error readout averaged over various sampling periods, record average PM tube currents, and seek relationships between these values and other system parameters (such as receiving aperture diameter). In addition, attempts were made to relate these data to atmospheric conditions. Although this procedure yielded some indication of system performance, it provided very little insight into either the nature of system operation, or the mechanism for the occurrence of errors. Furthermore, because of transmission variations in the atmospheric path lasting several seconds or minutes, there was considerable difficulty in obtaining correlation between the averaged bit error rate and other system parameters. For this reason, we felt it desirable to simultaneously monitor and record the bit error rate, the detector currents, and the mean square value of signal fluctuations.

In order to provide the field test receiver site with this capability, the instrumentation shown in Figure 2-7 was constructed. The custom designed circuits shown in this block diagram are the isolation amplifiers, power divider, and D/A error output converter.

The isolation amplifiers sample the current outputs of the photomultipliers and provide the DC and low frequency AC components (atmospheric induced fluctuations) to the strip chart recorder. The RMS voltmeter is coupled to the output of one amplifier so that the RMS current of one photomultiplier may be recorded.

The error output from the pseudo-random bit error detector is divided three ways to provide simultaneous inputs to a television monitor, frequency counter, and the D/A error output circuit. The D/A error output circuit integrates the error pulses in order to supply an analog output proportional to the bit error rate during the selected integration period.

2.2.3.1 Isolation Amplifiers

The isolation amplifiers are packaged within the receiver compartment. Because of the high frequency signal components on the photomultiplier outputs, it was necessary to locate these amplifiers close to the signal source. Although high frequency signal information is not used in the strip chart recording of average currents, long leads connected at this point would disrupt the signal, causing the bit error detector to malfunction. The isolation amplifiers shown in Figure 2-8 are integrated circuit operational amplifiers. Resistive isolation to the photomultiplier output is provided by the 100 K to 1 KΩ feedback network around the amplifier. Enough gain is provided in the amplifier, from DC to 10 kHz, so that the output is the same as that at the photomultiplier. This circuit provides a means of recording signal fluctuations and average current with only 0.01 percent loading on the signal input to the preamplifier, and less than 3.0 percent loading on the DC current to the front panel current monitoring meters.

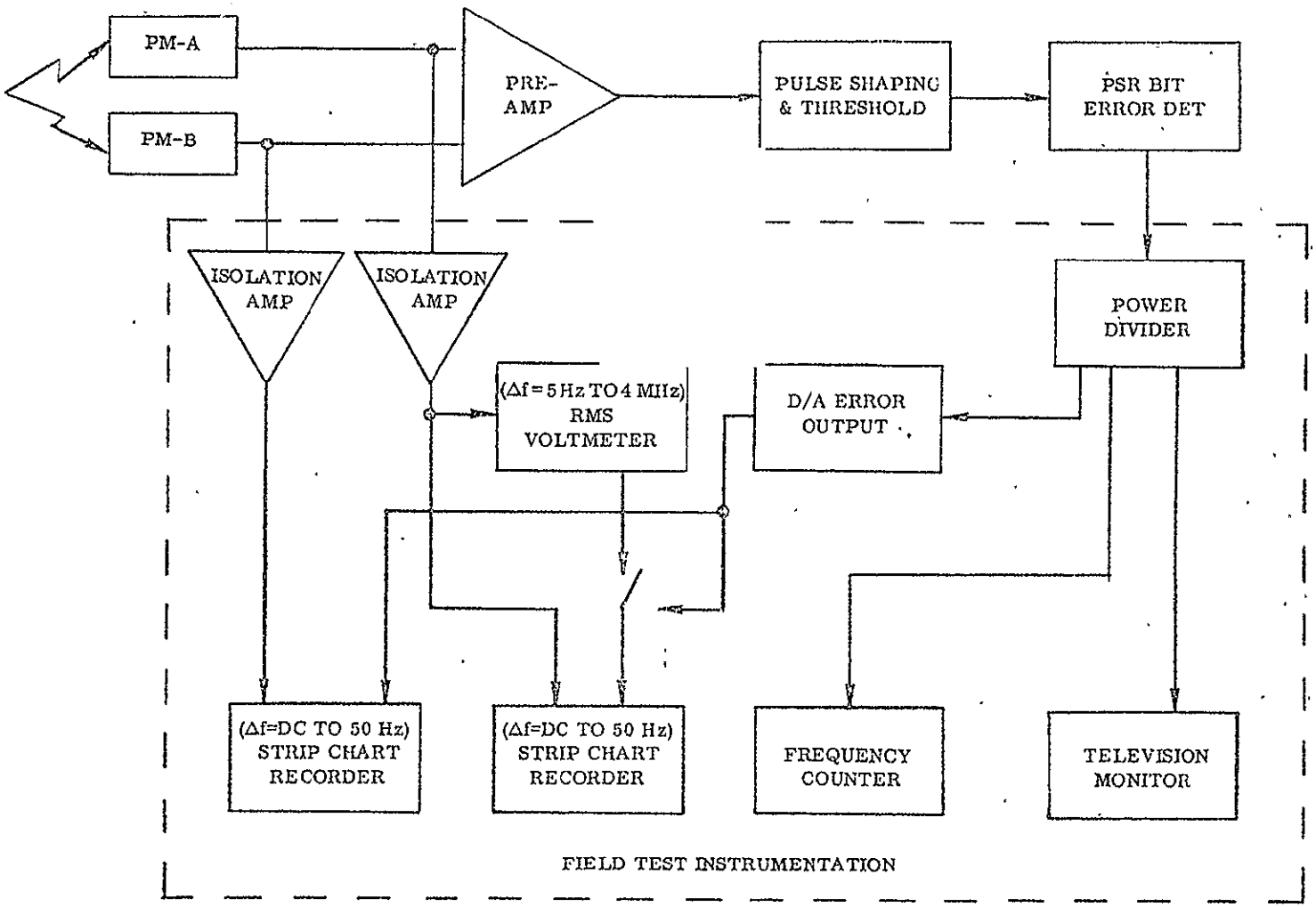

Figure 2-7. Optical Communications Receiver Set

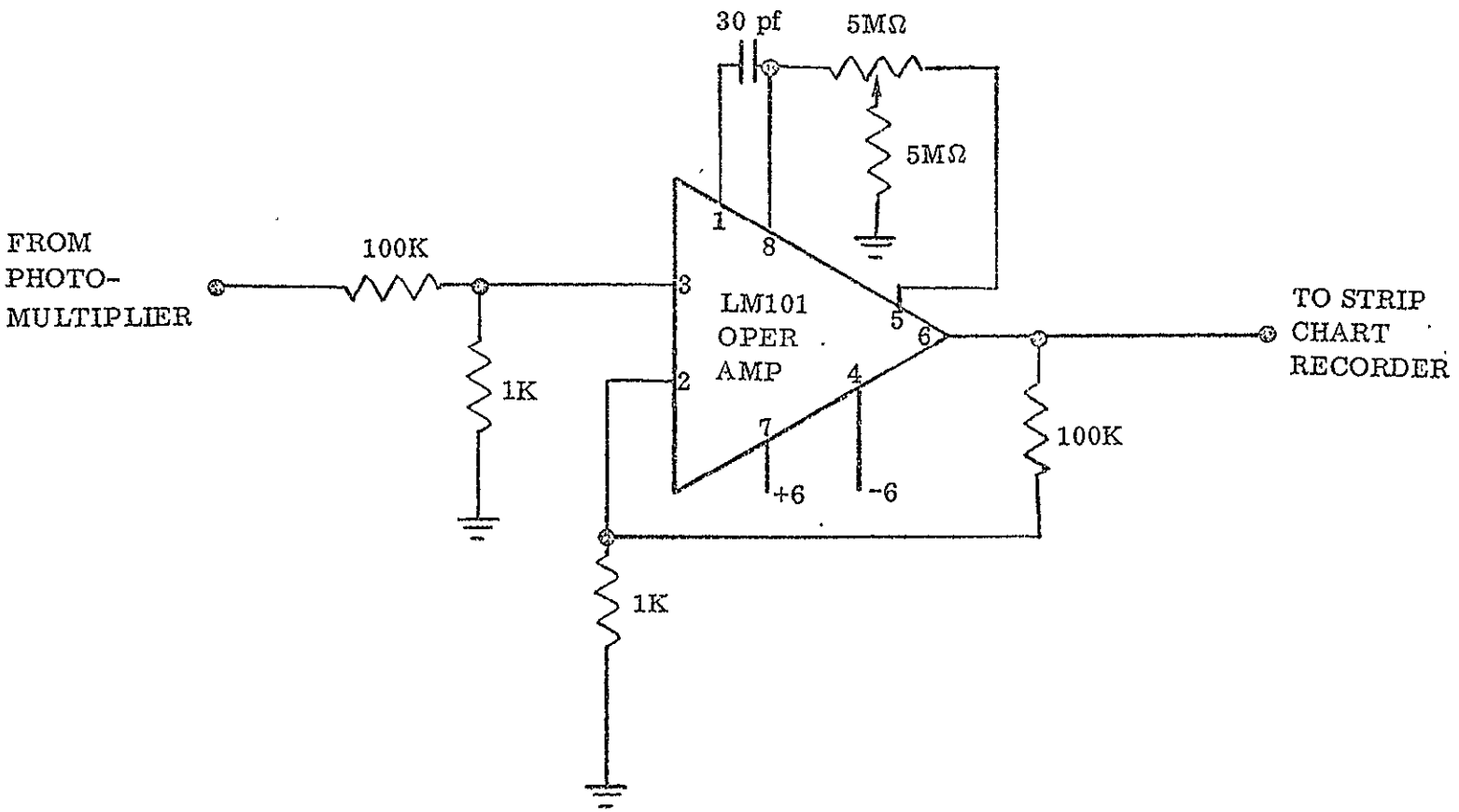

Figure 2-8. Isolation Amplifier for Scintillation and Average Current Monitoring.

2.2.3.2 Power Divider-Bit Error Detector Output

The Power Divider was designed to provide separate outputs from the bit error detector to the television monitor, frequency counter, and the D/A error output converter. The television monitor gives a coarse indication for system alignment, while the frequency counter provides average error rate and fine tuning information. The circuit shown in Figure 2-9 provides the three necessary outputs. Two of the outputs are 0 to 1.2 V, as are required for the test equipment inputs, while the third output is 0 to +6 V, the level required by the D/A error output converter. The digital error output from the bit error detector is coupled to the base of transistor Q1, which is an amplifier switch that drives Q2 and Q3. Q2 provides outputs for the television monitor and frequency counter, while Q3 supplies a single DC coupled output to the D/A error converter. All outputs are 75Ω and are terminated at the far end of the line.

2.2.3.3 Digital to Analog (D/A) Error Output Converter

The D/A error converter shown in Figure 2-10 consists of an integrator, followed by an operational amplifier with a switch stepped gain control. This circuit accepts the bit error output from the power divider and converts it to a proportional DC output. The integrator design was based upon the response of the strip chart recorder that this unit drives. The strip chart recorder has a 3 db bandwidth of 50 hz, and the RC time constant of the integrator was set to fall off at 16 Hz. Such a bandwidth assured that the recorder would follow any changes in input with minimum distortion. The strip chart recorder sensitivity was set so that maximum amplifier output would give full scale readings for each sensitivity range. The amplifier gain was calculated for the full scale sensitivities corresponding to error rates of 10^{-5} through 10^{-1} in five steps. Therefore, an amplifier output of 10 volts on the least sensitive scale corresponds to an input error rate of 10^{-1} or 3 MHz, while a 1 volt

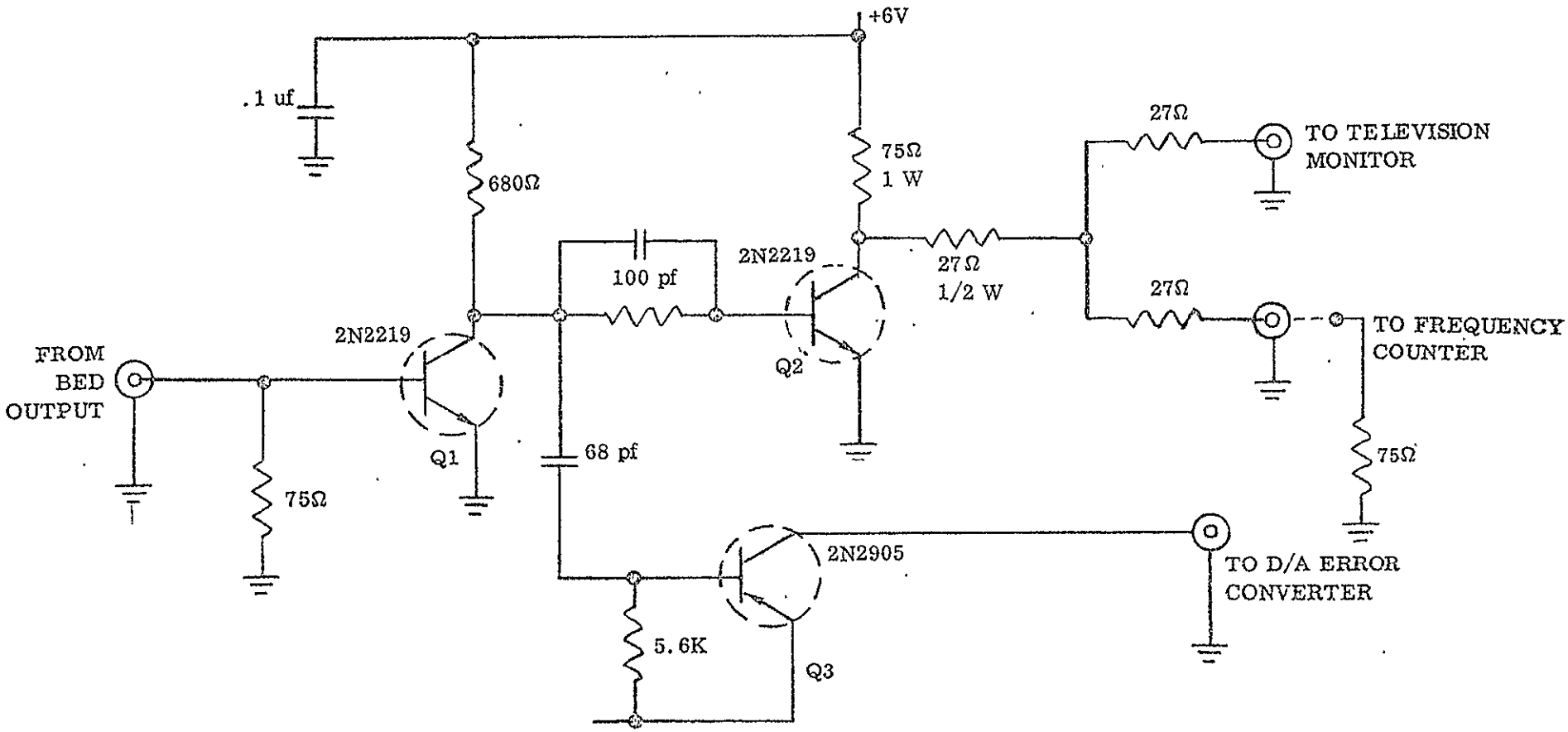

Figure 2-9. Power Divider (Bit Error Detector Output).

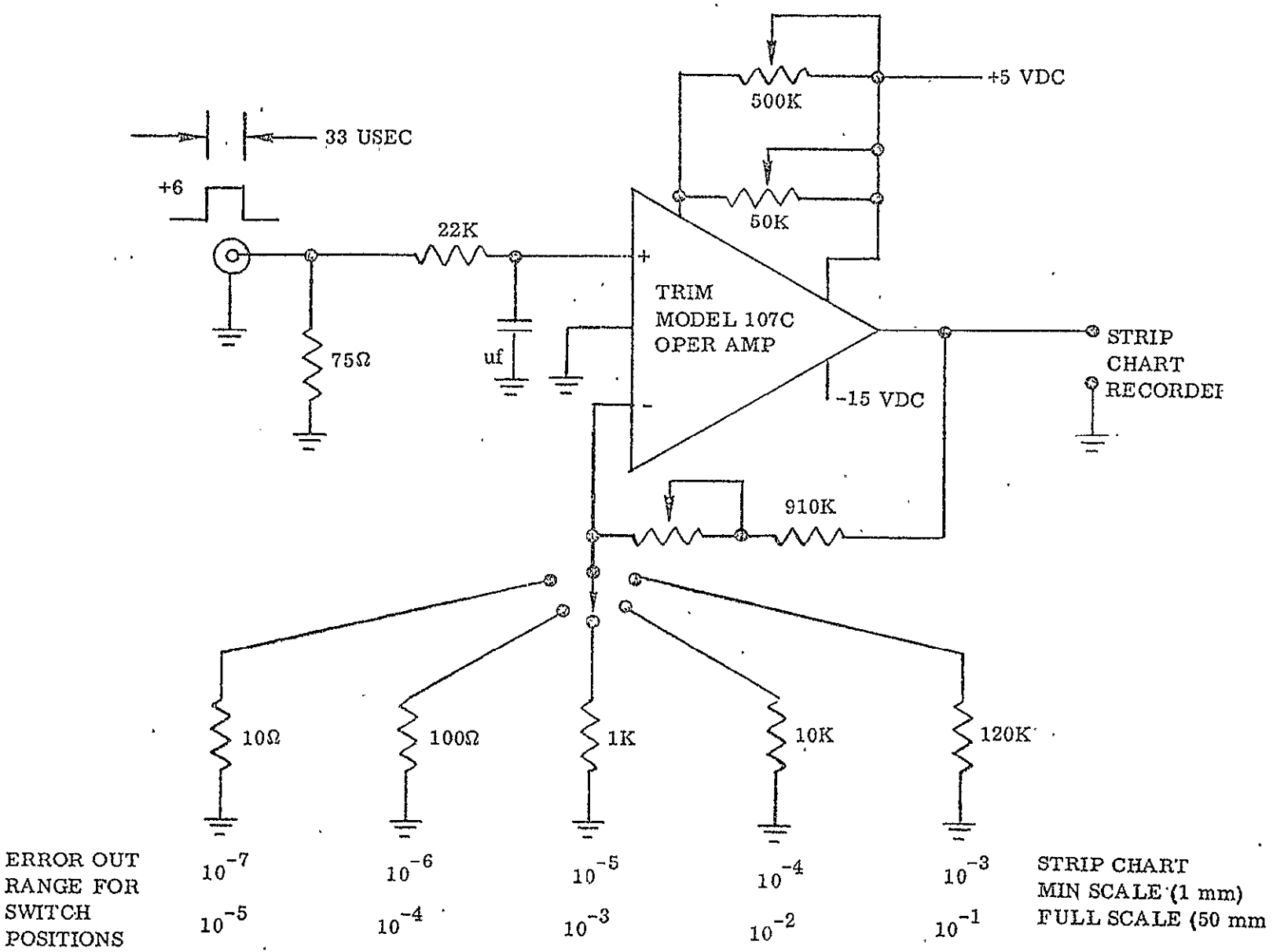

Figure 2-10. Digital-to-Analog Error Output Converter.

output corresponds to a 10^{-2} or 300 kHz error rate, and a 0.1 volt output corresponds to a 10^{-3} or 30 kHz error rate. In like manner, each successive switch position gives an order of magnitude greater sensitivity. On the most sensitive scale the error rate becomes so low with respect to the integration time that the amplifier output is a DC pulse for each error pulse received at the input. Between 10^{-6} and 10^{-5} error rate, the repetition rate is high enough to give a constant DC output. This unit was tested and calibrated with a pulse generator capable of delivering 33 nanosecond pulses at bit rates of 3 per second to 3 million per second.

3.0 SYSTEM MATHEMATICAL MODEL

In the following paragraphs a mathematical model is developed for use in predicting potential performance of the Optical Communications System. First discussed is the ideal system, one limited by only the most fundamental types of noise. This ideal model is then modified to include the most common sources of noise, encountered in photon-counting communications systems operating in the field.

3.1 PERFORMANCE OF AN IDEAL SYSTEM

An ideal optical communications system has its performance limited by design parameters (such as laser power, modulation index, collection aperture diameter, etc.) and the fundamental fluctuations in the detected signal due to photocurrent shot noise. This section is concerned with introducing both these system concepts and the analytical techniques that will be expanded later to form a general model.

3.1.1 Sensor Photocurrent and Its Variance

It is important to clarify first the term "modulation index." Figure 3-1 depicts a partially modulated binary pulse train. The peak amplitude of this pulse train is A_p, and the minimum amplitude is A_m. The average amplitude is $\bar{A} = (A_p + A_m)/2$, assuming a long random and equally likely series of binary pulses. The modulation index M is defined as

$$M = \frac{A_p}{\bar{A}} - 1 = \frac{A_p - A_m}{A_p + A_m} \qquad (3.1)$$

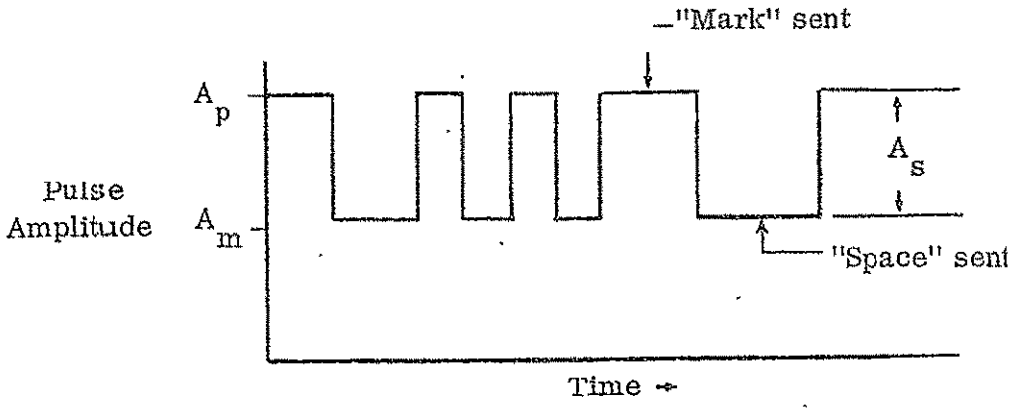

Figure 3-1. Partially Modulated Binary Pulse Train

In terms of the average amplitude $\bar{A}$, the peak amplitude can be written as $A_p = \bar{A}\,(M + 1)$. In a like manner the minimum amplitude A_m can be written as $A_m = \bar{A}\,(1 - M)$. The signal amplitude A_s is defined as the difference between the maximum and minimum amplitudes. Consequently, it follows that $A_s = A_p - A_m \doteq 2M\,\bar{A}$.

The amplitudes of Figure 3-1 may represent any of a number of types of information carriers. For instance, the peak amplitude A_p may represent peak numbers of photons, photoelectrons, photocurrent values, or other like quantities. In an ideal system, the average photoelectron current is directly proportional to the average radiation incident on the photosensor. Consequently, in using the system of subscripts introduced above with an average photoelectron current (electrons per second) of $\bar{i}$, the resultant expression that represents a mark having been sent is the term $(1 + M)\,\bar{i}$, and likewise, the photocurrent representing a space is $(1 - M)\,\bar{i}$.

The shot noise fluctuations in a photocurrent are well described by a Poisson statistical distribution. Hence, the statistical variance of the number of photoelectrons counted during a time interval Δt is proportional to the

product of the photocurrent, i_{pc}, and the sample period, Δt. In equation form,

$$i_p = (1 + M)\bar{i};\ i_m = (1 - M)\bar{i};\ \text{and}$$
$$\text{var}\{ i_{pc} \} = k\, i_{pc}\, \Delta t. \qquad (3.2)$$

The constant of proportionality, $k \geq 1$, is used to describe the noise effects of amplification, such as dynode noise in a multiplier phototube (Reference 2).

3.1.2 The Bit Error Rate (BER) and Its Effects

The product of the sample period, Δt, and the photoelectron current, i_{pc}, is the number, N, of electrons counted during a sample interval. The decision as to whether a space or mark was sent is made by comparing the number of photoelectrons counted with some threshold value N_t. If the number of electrons counted is greater than N_t, it is decided that a mark was sent. If the number counted is less than N_t, it is decided that a space was sent. Because of the variance in the values of i_{pc}, there is some statistical probability that, although a mark was sent, the product $i_{pc}\,\Delta t$ in the receiver will be less than N_t. Hence, the receiver logic circuitry will make an incorrect decision in such cases. The probability of making an incorrect decision during a sample interval is called the bit error rate (BER).

Although other factors such as signal-to-noise ratio could be used, bit error rate is more indicative of the quality of a digitally coded communications channel. For channels using non-digital modulation schemes, it is clear that the lower the system's potential bit error rate, the better the information transmission (as measured by fidelity, signal-to-noise ratio, or any other method), even though there is no linear relationship between these characteristics. The use of a system's potential bit error rate as a basis to judge its

performance provides the advantage of easily considering the adverse effects of many and varied noise factors as a whole. For example, some criteria of performance require that all noise sources, to be combined, must have similar frequency spectra. These analytical techniques would have difficulty in estimating the simultaneous effects of signal current shot-noise and atmospheric turbulence.

It is of value to compare the subjective quality of a closed circuit video picture as a function of bit error rate in the communications channel. Figure 3-2 shows the resultant degradation in received picture quality as the BER is increased from 10^{-5} to 0.30, by attenuating the radiation of the transmitted laser beam. These photos were taken during a laboratory test of the Optical Communications System.

3.1.3 Computation of the Ideal Single-Channel BER

In a single-channel photon-counting type of digital system, a mark or space decision is based upon whether or not the number of photoelectrons counted in one photosensor during a bit interval is larger than some threshold value, N_t. An error occurs when either: (1) a signal is sent but not detected or, (2) when the threshold value is exceeded during an interval when no signal is sent. In equation form, the probability of an error during a bit interval (the bit error rate) is

$$\begin{aligned} BER = {} & P\{\text{signal sent}\} \cdot P\{\text{noise and signal} \leq N_t\} \\ & + P\{\text{signal not sent}\} \cdot P\{\text{noise} > N_t\}. \end{aligned} \tag{3.3a}$$

Since in the random NRZ coding considered here, the probability of a signal being sent during a sample bit interval is 1/2, Equation 3.3a becomes

$$\begin{aligned} ER = {} & 1/2\ P\{\text{noise and signal} \leq N_t\} \\ & + 1/2\ P\{\text{noise} > N_t\}. \end{aligned} \tag{3-3b}$$

The derivation of the system bit error rate discussed here is concerned with only the variations in the signal amplitude itself. These fluctuations in the modulated and unmodulated portions of the collected laser beam are caused by the inherent photocurrent shot noise. Using the terminology of Sections 3.1.1 and 3.1.2, we correctly consider a mark to have been sent if the number of photoelectrons $\tilde{N}_p$ counted during a sample period is larger than the threshold value N_t. We correctly decide that a space has been sent if we detect a smaller value $\tilde{N}_m$. Both $\tilde{N}_p$ and $\tilde{N}_m$ are random variables becuase of the effects of photocurrent shot noise. Intuitively, the threshold value N_t should be set at some number between the average values of $\tilde{N}_p$ and $\tilde{N}_m$. One of the purposes of the following analysis is to determine the value of N_t which minimizes the system's bit error rate.

Equation 3.3 can be rewritten to include the variables $\tilde{N}_p$ and $\tilde{N}_m$ as

$$BER = \frac{1}{2} P\{\tilde{N}_p \leq N_t\} + \frac{1}{2} P\{\tilde{N}_m > N_t\}. \quad (3.4)$$

In terms of probability distributions, the components of the last equation are

$$P\{\tilde{N}_p \leq N_t\} = \int_{-\infty}^{N_t} dz\, P\{\tilde{N}_p = z\}, \quad (3.5a)$$

$$P\{\tilde{N}_m > N_t\} = \int_{N_t}^{\infty} dz\, P\{\tilde{N}_m = z\}. \quad (3.5b)$$

For large numbers of photoelectrons N the shot noise (Poisson) distributions are approximately normal.

Hence, keeping in mind that $\bar{N}(1+M)\Delta t = i_p$ and $\bar{N}(1-M)\Delta t = i_m$, we find that the combination of equations 3.2 and 3.5 results in

$$P\{\tilde{N}_p \le N_t\} = \int_{-\infty}^{N_t} dz \; \frac{e^{-\frac{1}{2}\left(\frac{z - \bar{N}(1+M)}{\sqrt{\bar{N}k(1-M)}}\right)^2}}{\sqrt{2\pi}\sqrt{\bar{N}k(1+M)}}, \tag{3.6a}$$

$$P\{\tilde{N}_m > N_t\} = \int_{N_t}^{\infty} dz \; \frac{e^{-\frac{1}{2}\left(\frac{z - \bar{N}(1-M)}{\sqrt{\bar{N}k(1-M)}}\right)^2}}{\sqrt{2\pi}\sqrt{\bar{N}k(1-M)}} \tag{3.6b}$$

We can use here the tabulated functions P and Q where:

$$P(r) = \frac{1}{\sqrt{2\pi}} \int_{-\infty}^{r} e^{-\frac{t^2}{2}} \, dt, \quad Q(r) = \frac{1}{\sqrt{2\pi}} \int_{r}^{\infty} e^{-\frac{t^2}{2}} \, dt; \tag{3.7}$$

so that Equation 3.4 for the bit error rate simplifies to

$$BER = \frac{1}{2} P\left(\frac{N_t - \bar{N}(1+M)}{\sqrt{k\bar{N}(1+M)}}\right) + \frac{1}{2} Q\left(\frac{N_t - \bar{N}(1-M)}{\sqrt{k\bar{N}(1-M)}}\right). \tag{3.8}$$

n this case, the bit error rate is minimized for a threshold value of

$$N_t = \bar{N}\sqrt{1-M^2}\left[1 + \frac{k}{2M\bar{N}} \ln\left(\frac{1+M}{1-M}\right)\right]^{\frac{1}{2}} \approx \bar{N}\sqrt{(1-M^2)}, \tag{3.9}$$

an approximation easily justified for large values of $\bar{N}$. With this optimum value of N_t, the bit error rate from Equation 3.8 is found to be

$$BER\Big|_{\substack{\text{Single} \\ \text{Channel,} \\ \text{Optimum}}} = Q\left[\sqrt{\frac{\bar{N}}{k}}\left(\sqrt{1+M} - \sqrt{1-M}\right)\right] \tag{3.10}$$

or approximately

$$Q\left[\sqrt{\frac{\bar{N}}{k}}\left(M + \frac{M^3}{8} + \frac{7M^5}{128} + \cdots\right)\right]$$

Equation 3.10 is plotted in Figure 3-3 for two values of modulation index M.

3.1.4 Computation of the Ideal Binary Channel BER

The system configuration for binary channel operation was shown in Figure 2-1b. Analysis of an ideally balanced binary system is somewhat simpler than that of the single channel, since there is no threshold value N_t to be considered. In this situation, the decision as to whether a mark or space was sent is based on which of two channels has the greater number of photoelectrons. Using subscripts 1 and 2 for the two channels, we can write the expression for the bit error rate, analogous to Equation 3.4, as

$$BER = \frac{1}{2} P\{\tilde{N}_{p_1} < \tilde{N}_{m_2}\} + \frac{1}{2} P\{\tilde{N}_{p_2} < \tilde{N}_{m_1}\} \qquad (3.11)$$

For a balanced symmetrical system, the two probabilities are equivalent, and we can write

$$BER = P\{\tilde{N}_{p_1} < \tilde{N}_{m_2}\} = P\{\tilde{N}_{p_1} - \tilde{N}_{m_2} < 0\}. \qquad (3.12)$$

Written in terms of conditional probability distributions, the last equation is

$$BER = \int_{-\infty}^{0} dz \int_{-\infty}^{\infty} dy \; P\{\tilde{N}_p = z + y\} \cdot P\{\tilde{N}_m = y\} \qquad (3.13)$$

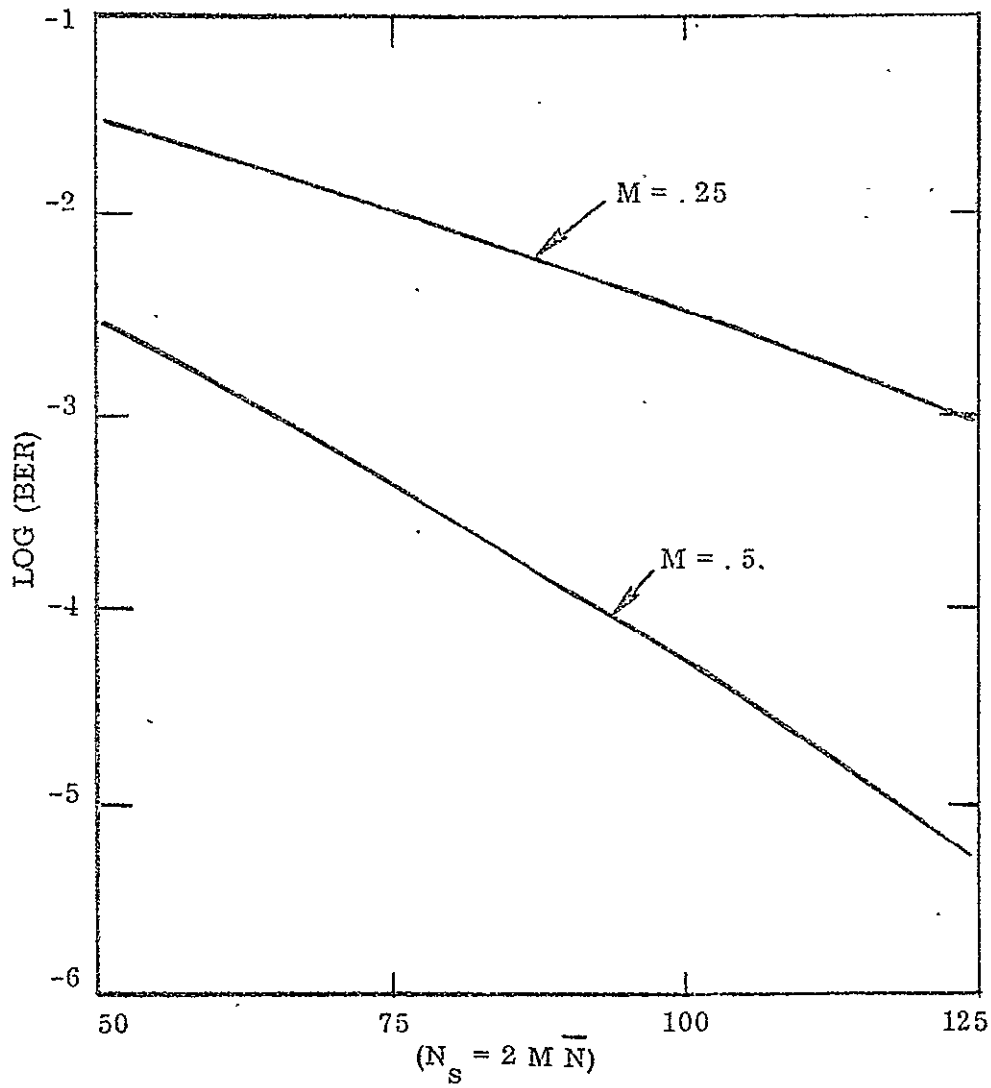

Figure 3-3. Single Channel Bit Error Rate (from Eq. 3.10). The factor k is 1.6.

Approximating the probabilities with normal distributions, as was done with Equation 3.6, the last expression can be arranged in explicit form as

$$BER = \int_{-\infty}^{0} dz \int_{-\infty}^{\infty} dy \; \frac{e^{-\frac{1}{2}\left(\frac{z+y-\bar{N}(1+M)}{\sqrt{k\bar{N}(1+M)}}\right)^2}}{\sqrt{2\pi}\sqrt{k\bar{N}(1+M)}} \cdot \frac{e^{-\frac{1}{2}\left(\frac{y-\bar{N}(1-M)}{\sqrt{k\bar{N}(1-M)}}\right)^2}}{\sqrt{2\pi}\sqrt{k\bar{N}(1-M)}} . \quad (3.14)$$

This equation, where $\bar{N}$ is the product $i_{pc}\,\Delta t$ averaged on one photosensor, can be integrated directly to obtain the simpler form

$$BER\Big|_{\substack{\text{Binary}\\ \text{Channel,}\\ \text{Optimum}}} = Q\left(M\sqrt{\frac{2\bar{N}}{k}}\right) \quad (3.15)$$

The last equation is plotted in Figure 3-4 for modulation indices ranging from 0.3 to 0.8.

3.1.5 Comparison of Ideal Single Channel and Binary Channel Systems

The practical differences between a single channel system and a binary channel system are mainly in the added complexity involved in the binary system's receiver. It is interesting to consider how great an advantage is gained from this additional receiver complexity. Given that the two systems would have the same types of photosensors, modulators, etc., we can calculate the increase in remote terminal laser power required by a single channel system to equal the performance (BER) of a binary channel system. By comparing equations 3.10 and 3.15 we see that the single channel system's laser power must be increased by the factor

$$\text{Required Laser Power Increase} = 1 + \sqrt{1 - M^2} \quad (3.16)$$

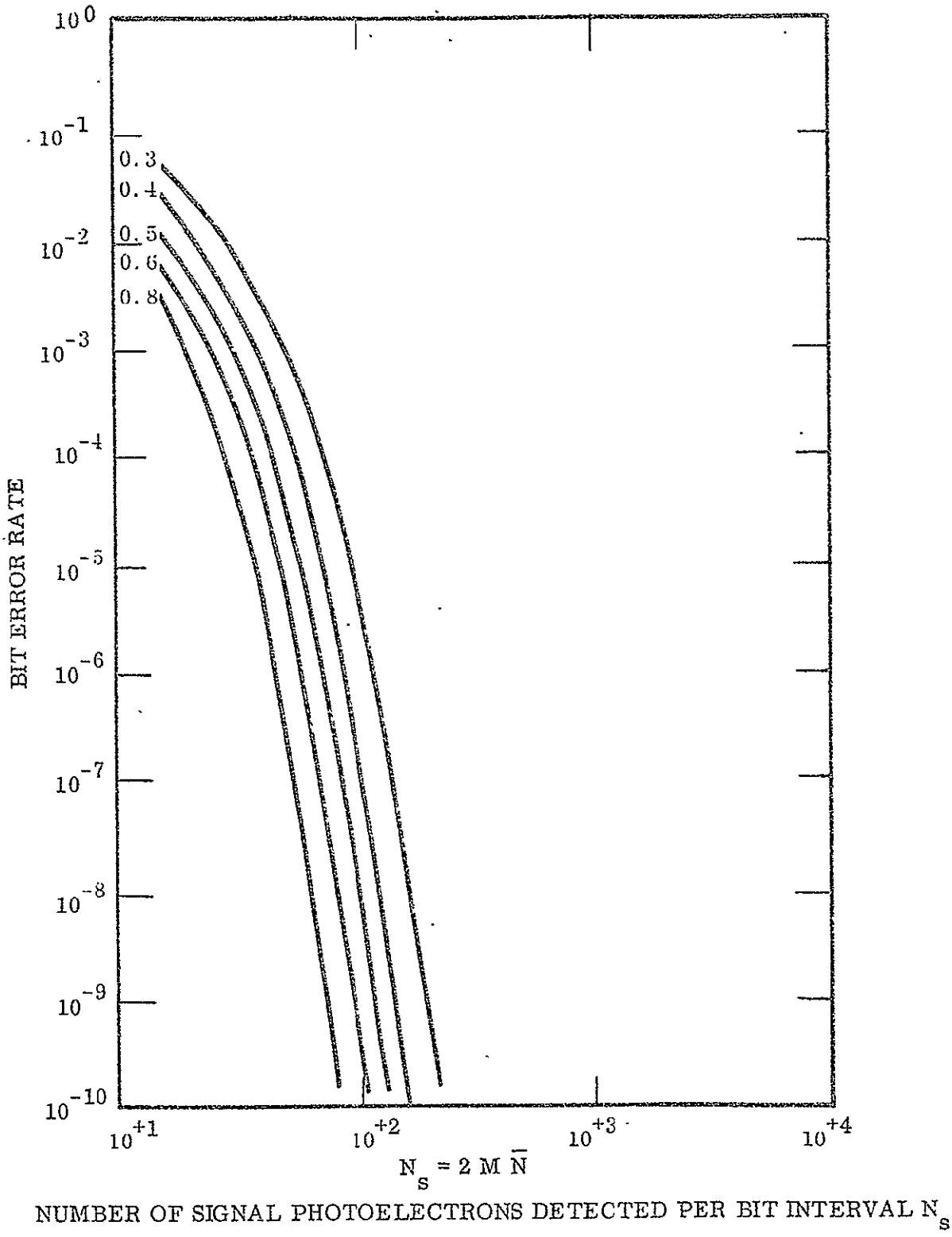

Figure 3-4. Binary Channel Bit Error Rate (from Eq. 3.15) With Modulation Index as the Parameter. The noise factor k is 1.6.

For example, if the modulator used were capable of a modulation index of 0.5, the required single channel laser power increase would be about 87 percent.

Equation 3.16 implies that both types of systems have about the same performance when used at high modulation indices and very low noise levels.

3.2 CALCULATION OF MODEL SYSTEM'S PERFORMANCE UNDER NOISY CONDITIONS

In the optical communications system under study there are seven principal sources of noise. For convenience in analysis, all seven may be considered together at the photodetector, even though some noise factors may not actually exist at that point in the signal processing train. Those noise factors not present at the photodetector (such as noise in later amplifiers) can be replaced in analysis with an equivalent noise generator at the photodetector. The eight principal noise factors occurring in the system under study are as follows:

a. Laser Generation Noise - a time varying factor multiplying the average radiative power from the laser. These fluctuations in laser power may be caused by power supply ripple, microphonics, etc.

b. Atmospheric Scintillation Effects - these act in much the same manner as the Laser Generation noise above, but of course with different frequency and probability distributions.

c. Signal and Background Shot Noise - variations in the photoelectron current that are proportional to the square root of the current.

d. Background Modulation - a factor usually encountered in scanning systems, in which the background noise may be much greater than that predicted by shot noise calculations.

e. Dark Current - in the system's photodetector, normally of concern only when operating with infrared sensitive sensors at low signal levels.

f. Dynode noise - significantly increases the fluctuations in photoelectron current during the first stages of amplification. If an electron multiplier type phototube were not used as the photosensor, the preamplifier would then be an important source of noise of this type.

g. Johnson or Thermal Noise - usually of concern only if the sensor's load resistor preceeds most of the signal amplification.

3.2.1 Sensor Photocurrent and Its Variance

In a two level digital signal as was pictured in Figure 3-1, the seven noise factors discussed above can be combined into multiplicative and additive contributions to the sensor photocurrent, i_{pc}. For the condition of a "mark" being sent, the signal photocurrent i_p and its variance are described, as was done with Equations 3.2, by

$$i_p = a(1 + M)\,\bar{i} + \sum i_n;\ \hat{N}_p = i_p \Delta t$$

$$\text{var}\,(i_{pc}) = k\, i_p \Delta t = k\, \hat{N}_p \qquad (3.17a)$$

For the conditions of a "space" being sent, the last equations take the form

$$i_m = a(1 - M)\,\bar{i} + \sum i_n;\ \text{var}\,(i_{pc}) = i_m \Delta t = k\, \hat{N}_m. \qquad (3.17b)$$

In the last equations, i_{pc} is the instantaneous photocurrent (in electrons per second) and the term a is the product of factors describing system radiometry, time varying atmospheric scintillation, and laser generation noise effects. The last term $\sum i_n$, represents the sum of the DC noise currents, such as background and detector dark current. In the equations for the photocurrent variance, var (i_{pc}), the coefficient k describes multiplicative amplifier or dynode noise, and as before, Δt represents the time interval over which the photocurrent is sampled.

3.2.2 General Form for the BER of a Noisy System

But for an added complexity in the component equations 3.5, the derivation of the system BER using equations 3.17 follows that of equation 3.2. In regards to the previous ideal system, it was assumed that the average signal irradiance on the photosensor was constant. Variations in the photoelectron current were due to shot noise alone. However, in the situation where the system suffers from phenomena such as atmospheric scintillation and its resultant time varying effects, the major variations in the sensor photocurrent can be due to similar variations in the signal irradiance on the photodetector. Hence the term $P\{\tilde{N}_p = z\}$ in Equation 3.5a must be replaced with a more complex statistical expression. The term $P\{\tilde{N}_p = z\}$ is the probability that "z" photoelectrons will be counted during a sample interval if a "mark" is sent, and the long-term average number of photoelectrons counted is $\bar{N}$. However, in the presence of scintillation or fluctuating laser power, $\bar{N}$ is not constant and must be replaced by a random variable $\tilde{N}$. The shot noise in the photocurrent still exists, but a parameter of its distribution i. e., the population mean, is also a variable. For this reason we have a conditional distribution $P\{\tilde{N}_p = z; x\}$. This expression represents the probability that the number of photoelectrons counted for a "mark" sent be z, given that the mean number $\tilde{N}$ is x. It can be seen that the original expression for $P\{\tilde{N}_p = z\}$ is replaced by

$$P\{\tilde{N}_p = z\} = \int_{-\infty}^{\infty} dx\, P\{\tilde{N}_p = z; x\} \cdot P\{\tilde{N} = x\} \qquad (3.18)$$

As a consequence, the form of Equations 3.5 for a single channel BER is changed to

$$P\{\tilde{N}_p \le N_t\} = \int_{-\infty} dx \int_{-\infty}^{t} dz \; P\{\tilde{N}_p = z; x\} \cdot P\{\tilde{N} = x\} \quad , \qquad (3.19a)$$

$$P\{\tilde{N}_m > N_t\} = \int_{-\infty}^{\infty} dx \int_{N_t}^{\infty} dz \; P\{\tilde{N}_m = z; x\} \cdot P\{\tilde{N} = x\} \quad . \qquad (3.19b)$$

These, combined with Equation 3.4, describe the BER for a single channel system with additive and multiplicative noise.

To describe the BER for the binary channel system in a noisy environment, an expression similar to Equation 3.13 can be derived. Hence, written in terms of conditional probability distributions,

$$BER\Big|_{\substack{\text{Binary}\\ \text{Channel}}} = \int_{-\infty}^{0} dz \int_{-\infty}^{\infty} dy \int_{-\infty}^{\infty} dx \; P\{\tilde{N}_p = z + y; \tilde{N} = x\} \cdot P\{\tilde{N}_m = y; \tilde{N} = x\} \cdot P\{\tilde{N} = x\}. \qquad (3.20)$$

Equations 3.19 and 3.20 describe system BER with statistical expressions. In order to obtain numerical values, these terms must be replaced with algebraic expressions. The most important additional source o noise to be considered here is that due to atmospheric scintillation. It is well known (Reference 3) that these turbulence induced statistical variations in beam transmittance do not follow the normal probability distribution. For this reason, the next section digresses somewhat to discuss the log-normal distribution, which is more appropriate for use in modeling atmospheric effects.

3.2.3 Log-Normal Probability Distribution

The log-normal probability distribution (Reference 4) is applied in situations where a series of independent random impulses c_j have effects on a phenomenon which are dependent on the instantaneous state x_j of the phenomenon.

Furthermore, the magnitude of the change in state of the phenomenon, $x_{j+1}-x_j$, is proportional to the magnitude of the impulse c_j and some function $f(x_j)$ of the instantaneous state. Here the state x_j of the phenomenon was produced by c_{j-1}. The equation for the effect of c_j is

$$x_{j+1}-x_j = c_j\, f(x_j) = \Delta x_j \tag{3.21}$$

In the present application, we consider the change (Δx_j) to be a variation in the radiant power transmitted by a turbulent atmosphere, and this variation to be equal to the product of the radiant power itself, i. e., $f(x_j) = x_j$, and the magnitude of a number of turbulent impulses c_j. As a consequence we can rearrange the last equation to obtain the form

$$c_j = \frac{\Delta x_j}{f(x_j)} = \frac{\Delta x_j}{x_j} \tag{3.22}$$

The sum $C = \Sigma_j c_j$ of a large number of impulses, which we assumed above to be independent, tends to have a normal distribution as implied by the central limit theorem. If each of the impulses c_j has only a very slight effect Δx_j, then the resulting state x_n caused by a very large number of impulses c, is

$$\sum_{j=0}^{n} c_j = \sum_{j=0}^{n} \frac{\Delta x_j}{x_j} \approx \int_{x_o}^{x_n} \frac{dx}{x} = \ell n \frac{x_n}{x_o} \tag{3.23}$$

which, in the limit, has a logarithmic relationship to the impulses. Hence, we have a reasonable justification for writing the relationship

$$\ell n\, x = u, \tag{3.24}$$

where x is a linear function of the instantaneous radiant flux transmitted through the atmosphere, and u is a normally distributed variable dependent on the characteristics of the atmospheric turbulence.

To relate the characteristic parameters of x to those of u, we assume the variate u to have a mean m and a variance σ^2. The distribution function of u is

$$P\{u \le U\} = \int_{-\infty}^{U} du \; \frac{e^{-\frac{(u-m)^2}{2\sigma^2}}}{\sqrt{2\pi\,\sigma^2}} \tag{3.25}$$

The distribution function of x, $\Phi(x)$, can be determined from Equation 3.25, since from Equation 3.24, x is a function of the random variable u. With the appropriate change of variables we find that

$$P\{x \le X\} = \Phi(X) = \int_{0}^{X} \frac{dx}{x} \; \frac{e^{-\frac{(\ell_n x - m)^2}{2\sigma^2}}}{\sqrt{2\pi\,\sigma^2}} \; ; \; X \ge 0 \, . \tag{3.26}$$

The mean or expected value E(x) of the variable x is given by the Stieltjes - integral

$$E(x) = \int_{0}^{\infty} x \, d\Phi(x) = \exp\left[m + \frac{\sigma^2}{2}\right] \tag{3.27}$$

In a similar manner the expected value of x^2 can be found to be

$$E(x^2) = \exp\left[2\,m + 2\sigma^2\right] \, . \tag{3.28}$$

The variance of x is found from the well-known relationship

$$\text{Var}\{x\} = E(x^2) - E^2(x) = e^{2m+\sigma^2}\left[e^{2} - 1\right] \tag{3.29}$$

which leads directly to

$$\sigma^2 = \ell n\left[1 + \frac{\text{Var }\{x\}}{E^2(x)}\right] = \ell n\left[1 + \rho^2\right] \tag{3.30}$$

where

$$\text{Var }\{x\} = \rho^2 E^2(x)$$

It is convenient to work with the normalized variable x/E(x), which also has a log-normal distribution. In terms of the original parameters m and σ, we find that

$$E\left[\ell n \frac{x}{E(x)}\right] = m - \left(m + \frac{\sigma^2}{2}\right) = -\frac{\sigma^2}{2} \tag{3.31}$$

and

$$\text{Var}\left\{\ell n \frac{x}{E(x)}\right\} = \text{Var}\left\{\ell n(x)\right\} = \sigma^2 \tag{3.32}$$

The ratio x/E(x) may be considered here to describe the instantaneous transmittance of the atmosphere between the remote and base terminals. Averaged over a sample interval, the photocurrent, i, and the number of photoelectrons counted, $\tilde{N}$, are related to the variable x above as

$$\frac{\tilde{N}}{\bar{N}} = \frac{\tilde{i}}{\bar{i}} = \frac{x}{E(x)} \tag{3.33}$$

The distribution function for $\tilde{N}$ is

$$\Phi(x) = P\{\tilde{N} \le x\} = \int_0^x \frac{dx}{x\sqrt{2\pi\sigma^2}} \exp - \left[\frac{\ell n\, x - m}{\sqrt{2\sigma^2}}\right]^2 . \tag{3.34}$$

Using Equation 3.27 and the expression $E(\tilde{N}) = \bar{N}$, we find that the probability function for $\tilde{N}$ is

$$\frac{d\Phi}{dx} = g(x) = \frac{1}{x\sqrt{\pi}} \exp - \frac{1}{2}\left[\frac{\sigma}{2} + \frac{1}{\sigma} \ln \frac{x}{\bar{N}}\right]^2 , \tag{3.35}$$

$$g(x) = 0, \; x<0$$

where:

$$\sigma^2 = \ln\left[1 + \frac{\text{Var}\{\tilde{N}\}}{\bar{N}^2}\right] \tag{3.36}$$

3.2.4 Atmospheric Scintillation Effects - Typical Values

The principal signal fluctuations encountered in a space-to-space optical communications link are those due to the impressed modulation and fundamental photocurrent shot noise. However, in a satellite-to-ground terminal situation, atmospheric scintillation along the space-to-earth link is expected to influence the system's bit error rate to a great extent, dominating the simpler effects of photocurrent shot noise.

From Reference 5, we see that typical values for the log-amplitude variance, $C_\ell(0)$, for an optical path along the zenith angle Ψ are estimated to be fairly well represented by the equation $C_\ell(0) = 0.73 (\sec \Psi)^{11/6}$. The coefficient 0.73 of course varies from day to day for different locations, and for most astronomical observations, is probably too large. The variance, $\text{Var}\{P_c\}$, of the detected beam's radiant power P is related to $C_\ell(0)$ by the equation

$$\text{Var}\{P_c\} = P^2 \Theta\left[\exp\{4 C_\ell(0)\} - 1\right] = P^2 \rho^2 \tag{3.37}$$

where Θ is a complex function of the collector diameter, optical wavelength, and log-amplitude variance. Values of Equation 3.37 for collector diameters

of 50, 100, and 150 cm are shown in Figure 3-5. It is clear that the relative fluctuations represented by the normalized variance ρ^2 in the collected radiant power will affect both the modulated and the unmodulated portions of the beam from the satellite terminal.

Figure 3-6 illustrates the effect of atmospheric scintillation on the transmitted signal. Figure 3-6a depicts the digitally coded laser beam, with a modulation index of 0.5 and average amplitude $\bar{A}$. The relative fluctuations in the effective transmittance of the atmospheric path are shown in Figure 3-6b. For purposes of illustration, these fluctuations are pictured as varying at megahertz rates. In an actual system, these atmospheric scintillations would be concentrated below 100 hertz and would vary extremely slowly compared to the data rate. Figure 3-6c illustrates the resultant signal amplitude as collected by the ground terminal. The modulation index itself is unchanged from that of the transmitted beam in Figure 3-6a.

3.2.5 Noisy Single and Binary Channel BER

We may use the variable $x = a\bar{i}\Delta t$ in Equation 3.17 to obtain the diffinitions:

$$\begin{aligned} \hat{N}_p &= (1 + M)x + \Sigma i_n \Delta t \\ \hat{N}_m &= (1 - M)x + \Sigma i_n \Delta t \end{aligned} \tag{3.38}$$

With these substitutions, Equation 3.35 can be used to rewrite Equations 3.19 in the more general form:

$$P\{\tilde{N}_p \le N_t\} = \int_{-\infty}^{N_t} dz \int_0^{+\infty} dx\, g(x)\, \frac{e^{-\frac{1}{2}\left(\frac{z - \hat{N}_p}{\sqrt{k\hat{N}_p}}\right)^2}}{\sqrt{2\pi}\sqrt{k\hat{N}_p}} \tag{3.39a}$$

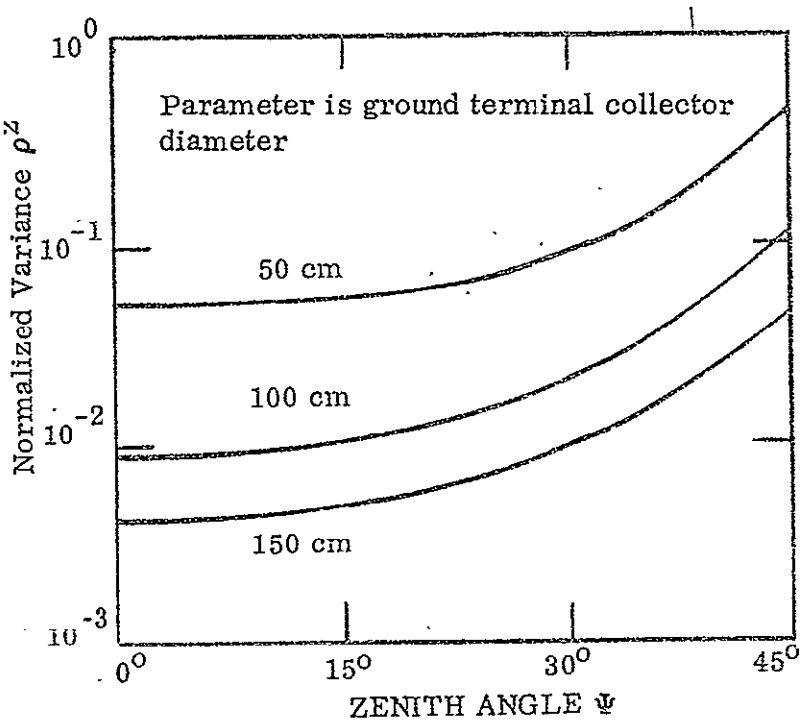

Figure 3-5. Variation in Scintillation Normalized Variance ρ^2 with Zenith Angle Ψ, as Evaluated from Equation 3.37.

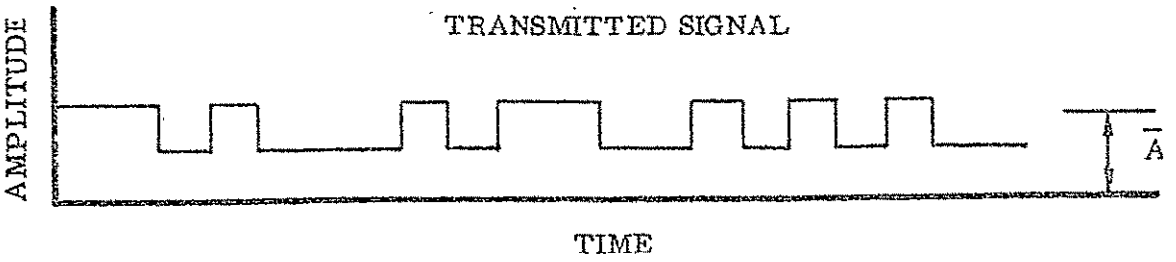

Figure 3.6a

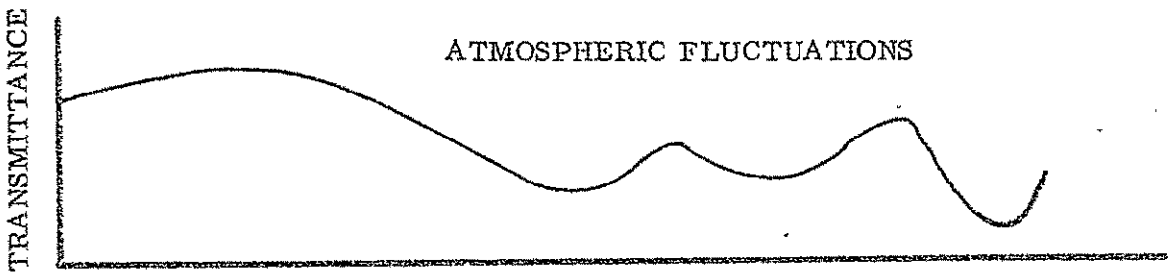

Figure 3.6b

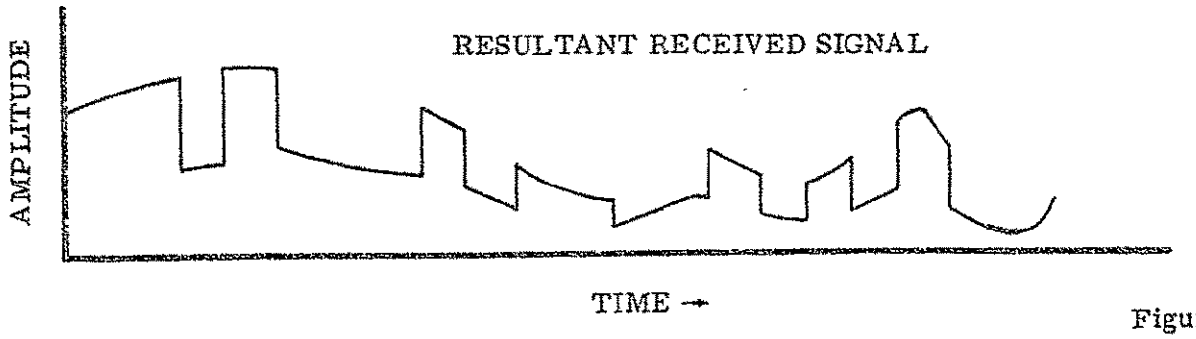

Figure 3.6c

Figure 3-6. Effects of Atmospheric Scintillation on a Digitally Coded Beam of Average Amplitude $\bar{A}$.

$$P\{\tilde{N}_m > N_t\} = \int_{N_t}^{\infty} dz \int_0^{+\infty} dx\, g(x) \frac{e^{-\frac{1}{2}\left(\frac{z-\hat{N}_p}{\sqrt{k\hat{N}_p}}\right)^2}}{\sqrt{2\pi}\sqrt{k\hat{N}_p}} \qquad (3.39b)$$

Using the expressions of Equation 3.7, we find that the noisy single channel BER is

$$\text{BER}\Big|_{\substack{\text{Single}\\\text{Channel}}} = \frac{1}{2}\int_0^{\infty} dx\, g(x) \left[P\left\{\frac{N_t - \hat{N}_p}{\sqrt{k\hat{N}_p}}\right\} + Q\left\{\frac{N_t - \hat{N}_m}{\sqrt{k\hat{N}_m}}\right\}\right]. \qquad (3.40)$$

The optimum value for the threshold setting N_t can be found by differentiation to be

$$N_t^2 = \hat{N}_m \hat{N}_p \left[1 + \frac{k \ln(\hat{N}_p/\hat{N}_m)}{\hat{N}_p - \hat{N}_m}\right],$$

or approximately

$$N_t \approx \sqrt{\hat{N}_m \hat{N}_p}. \qquad (3.41)$$

Hence, by substituting this value for the threshold into Equation 3.40 we obtain the simpler form

$$\text{BER}\Big|_{\substack{\text{Optimum,}\\\text{Single}\\\text{Channel}}} = \int_0^{\infty} dx\, g(x)\, Q\left[\frac{\sqrt{\hat{N}_p} - \sqrt{\hat{N}_m}}{\sqrt{k}}\right] \qquad (3.42)$$

In a similar manner, the expression for the balanced binary channel BER can be written from Equation 3.20 in explicit form as

$$\text{BER}\Big|_{\substack{\text{Balanced}\\\text{Binary}\\\text{Channel}}} = \int_{-\infty}^{0} dz \int_{0}^{\infty} dy \int_{0}^{\infty} dx\, g(x)\, \frac{e^{-\frac{1}{2}\left(\frac{z+y-\hat{N}_p}{\sqrt{k\hat{N}_p}}\right)^2}}{\sqrt{2\pi}\sqrt{k\hat{N}_p}} \cdot \frac{e^{-\frac{1}{2}\left(\frac{y-\hat{N}_m}{\sqrt{k\hat{N}_m}}\right)^2}}{\sqrt{2\pi}\sqrt{k\hat{N}_m}} \tag{3.43}$$

This expression may also be integrated to obtain the simpler form

$$\text{BER}\Big|_{\substack{\text{Balanced}\\\text{Binary}\\\text{Channel}}} = \int_{0}^{\infty} dx\, g(x)\, Q\left[\frac{\hat{N}_p - \hat{N}_m}{\sqrt{k(\hat{N}_p + \hat{N}_m)}}\right] \tag{3.44}$$

Equations 3.42 and 3.44 describe the performance of single and binary channel systems in the presence of additive noise. Measurements on the present optical communications system indicate that, in the laboratory and field tests performed, background noise and photosensor dark current are negligible i.e., $\sum_{i_n} \approx 0$. Representative values of system BER for these tests conditions are plotted in Figures 3-7 and 3-8 for a dynode noise factor of 1.6.

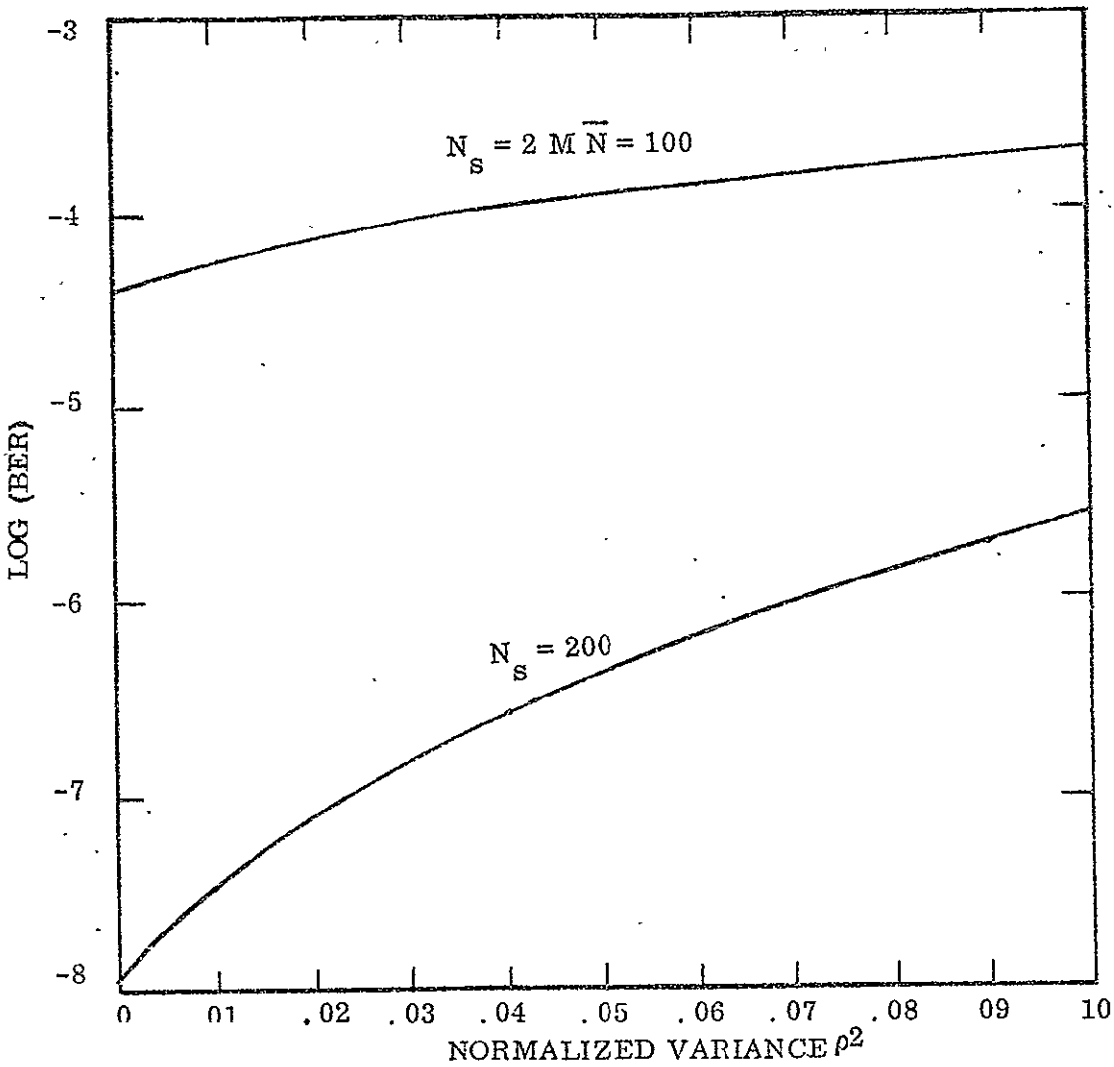

Figure 3-7. Single Channel Bit Error Rate in the Presence of Log-Normal Turbulence for k = 1.6 and M = 0.5, From Equation 3.42.

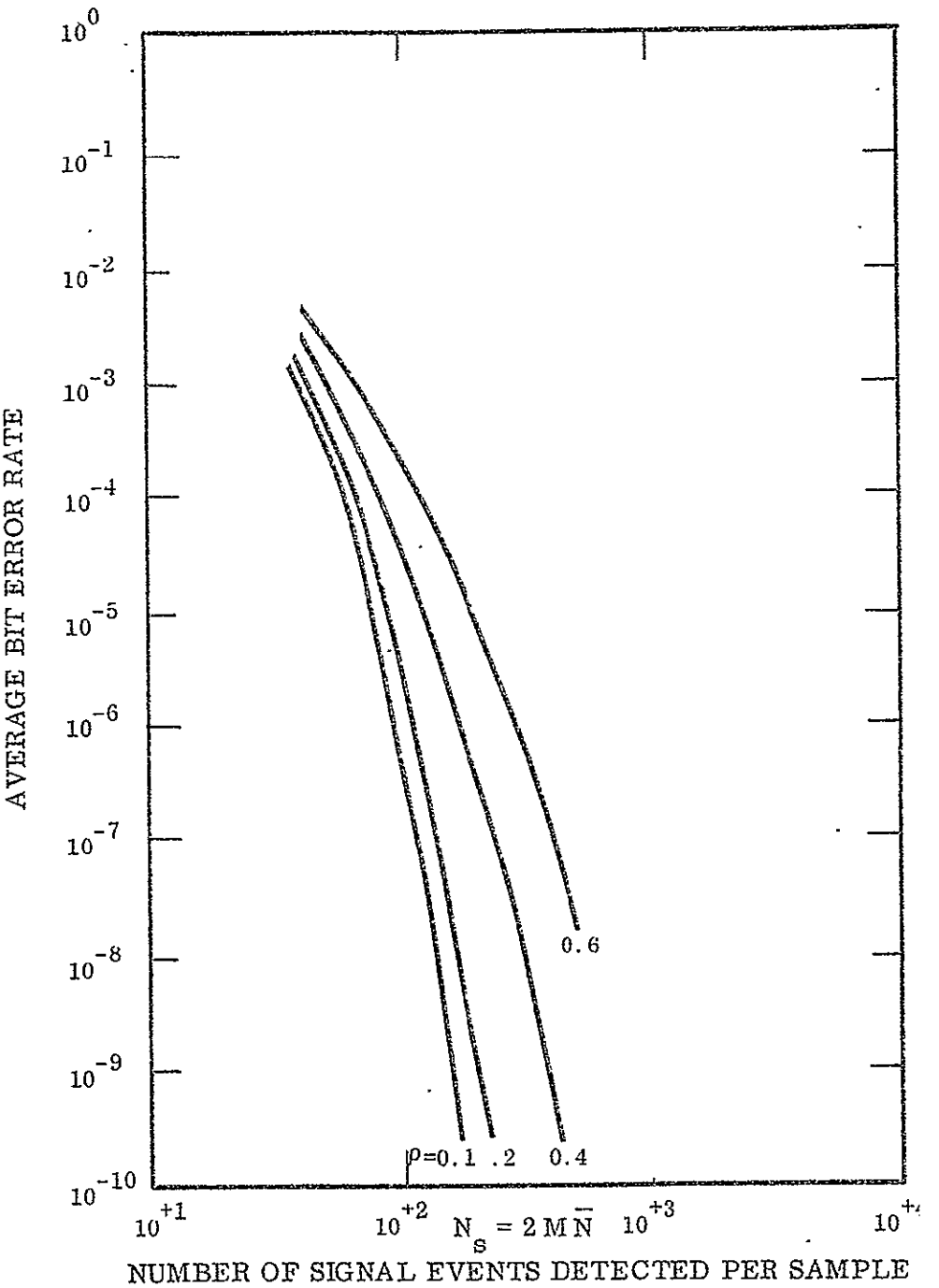

Figure 3-8. Binary Channel Bit Error Rate in the Presence of Lo
Normal Atmospheric Turbulence for k = 1.6 and M = 0.4,
From Equation 3.44.

4.0 SYSTEM EVALUATION

This section describes the experiments which were undertaken to test the Optical Communications System. The system was first evaluated in the relatively noise-free environment of the laboratory, In this situation, the resulting experimental data are comparable to that expected with the ideal system discussed in section 3.1. The optical communications package was then moved outside and operated in a real atmosphere. The data from these field experiments are compared with that of the noisy model of section 3.2.5.

4.1 LABORATORY EVALUATION

The Optical Communications System was first tested in a controlled laboratory environment to determine its potential information transmission capability. Variation in signal levels were achieved by attenuating the signal laser radiation with neutral density filters. Figure 4-1 shows, for single channel operation, the average bit error rate BER as a function of the mean number of photoelectrons $\overline{N}$ counted per sample interval, with modulation index M as a parameter. The values of M indicated were calculated from photosensor currents. These currents were measured at the detector load resistors with a sampling oscilloscope. Figure 4-2 compares single channel with binary channel operation. The BER values for an ideal system are also plotted for reference. It is noted that, for a given error rate, the number of events required in the single channel is approximately double the number of events in either channel in the binary configuration — which is what was anticipated from equation 3.16. It will also be noted that there is a rather constant

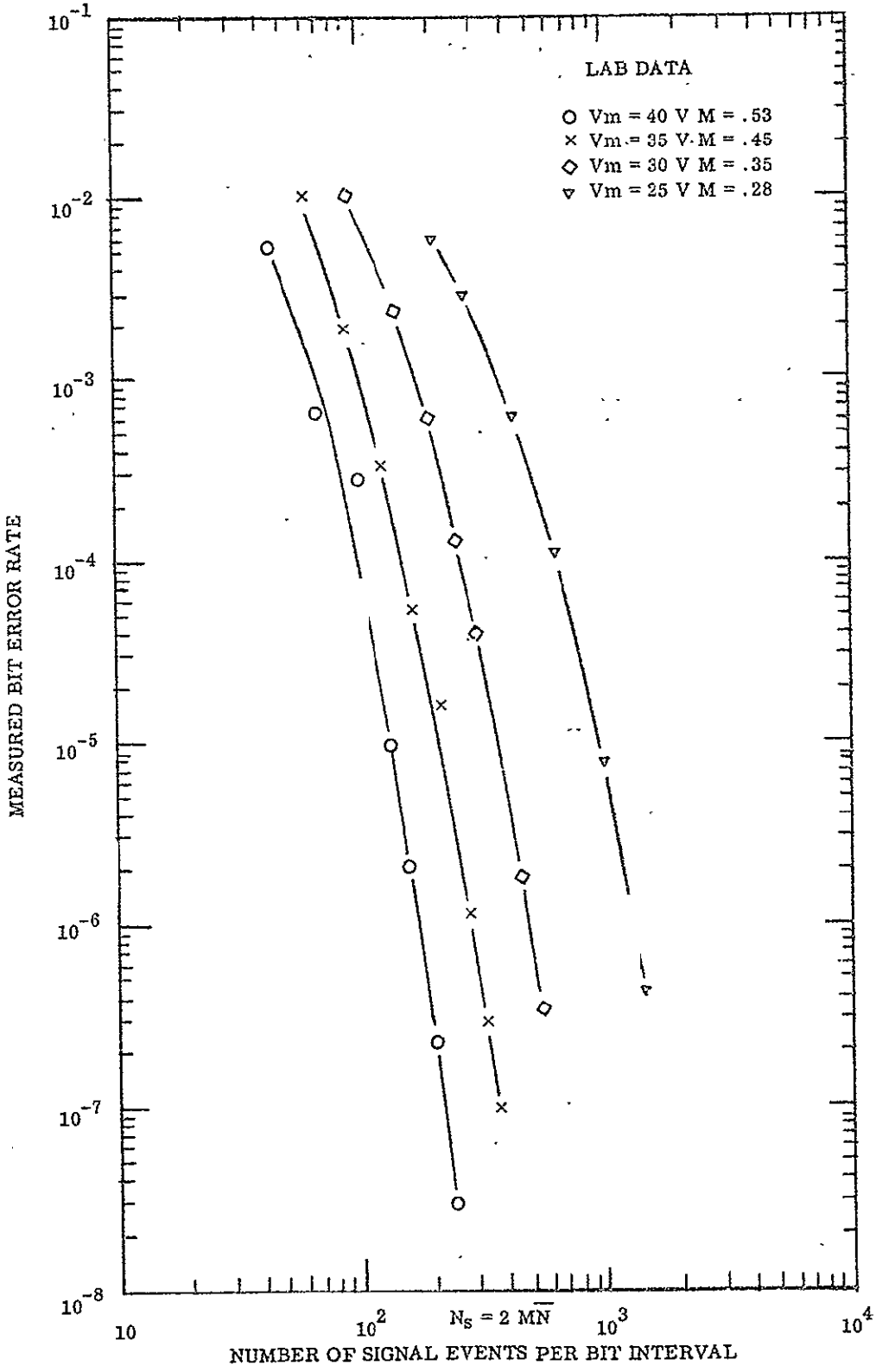

Figure 4-1. Single Channel Experimental Performance

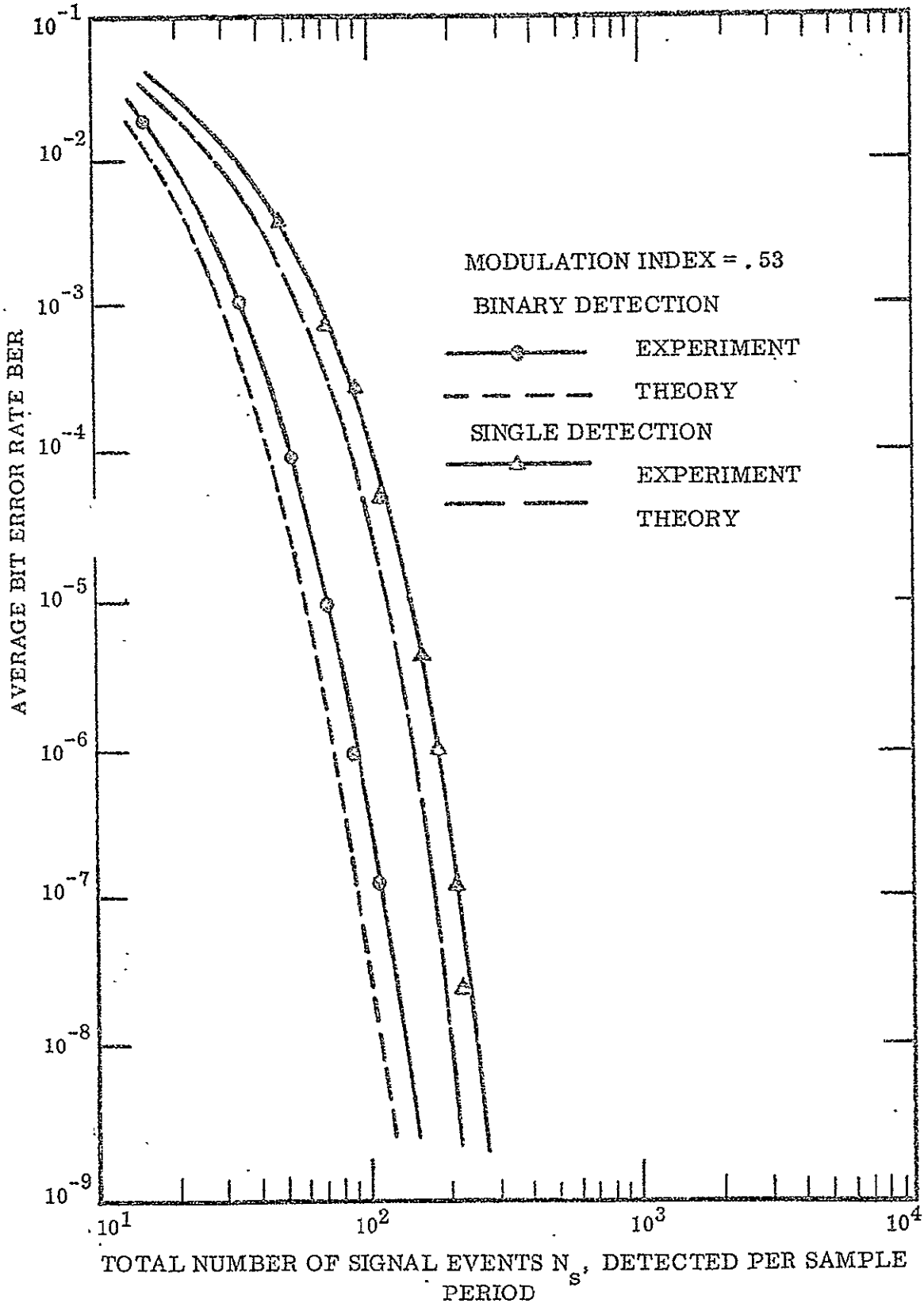

Figure 4-2. Comparison of Binary and Single Detection Channel Performance Experimental Data With The Model of Section 3.1.

20 percent difference between the experimentally measured and the theoretically necessary number of signal events required for a given bit error rate. The theoretical curves are quite similar to those of Figures 3.3 and 3.4, in which the photomultiplier dynode noise factor used was 1.6. Noise factors as high as five have been measured in some tubes, but, for the present equipment, the manufacturer was not asked for such data when the tubes were purchased.

4.2 FIELD TEST FACILITIES

Figure 4-3 shows the 5 mile test range that was used during the field evaluation. This slant path is inclined at only 6 degrees to the horizontal, and represents an extremely turbulent environment.

The color photo frontispiece of this report shows the ground terminal equipment, including a 22 in. diameter receiver telescope. The optical receiver is mounted to the rear of the telescope, and the processing electronics are contained in a rack to the side. The modulated laser beacon is mounted to the top of the receiving telescope and boresighted with the receiver unit. The purpose of the 22 in. aperture receiver is to study the effectiveness of large aperture averaging of atmospheric scintillations. The base terminal equipment is mounted on an aximuth-elevation type mount, indexed to the direction of the remote station so that the receiver can be pointed even though the transmitter site is not visible. Figure 4-4 shows the mobile laboratory facility used in field test experiments. This mobile laboratory is equipped with self-contained power supplies and meterological instrumentation for monitoring the condition of the atmosphere at the transmitter site. Figure 4-5 shows the remote terminal communications unit located in the mobile laboratory. The tracking/communications receiver section is shown to the left and the wideband digital transmitter section is on the right in the figure. This terminal is also mounted on a manually operated azimuth-elevation mount in order to coarsely point the unit to within the tracking receiver's one degree field-of-view.

..., ... 4-3. 5 Mile Test Range

Figure 4-4. Mobile Laboratories

Figure 4-5. Remote Terminal Inside Mobile Truck.

4.3 DATA FORMAT

Although many complex parameters affect the performance of an optical communications system, four factors are of major concern in the system's evaluation. These are: laser power, signal beam modulation index, atmospheric scintillation, and the resulting bit error rate. Figure 4-6 is a portion of a recording tape generated with the engineering model during a field experiment. The raw data shown here are the bases for calculations that lead to evaluating system performance.

The two curves in the upper portion of Figure 4-6 are measurements of anode current of the system's photomultiplier tube sensor. The straight line at the top of the figure is the system's zero or dark level. This current measurement is made with all radiation blocked from the photosensor, and is an indication of the tube's dark current. The second curve from the top is a record of the tube's output current and shows the noisy effects of atmospheric scintillation. This curve was generated on the 5 mile test range shown in Figure 4-3. The normalized variance determined from this data was $r = 0.31$, the term r being an experimental estimate of the parameter ρ of equation 3.30. The laser beam was heavily attenuated with neutral-density filters during this test run, limiting to 44 the average number of signal events per sample period.

The lowest curve of Figure 4-6 is a series of one second timing marks, used for setting the horizontal scale. The curve above these timing marks indicates the instantaneous system bit error rate, the output of the bit error detector of Figure 2-3. Under close inspection, it is seen that error bursts occur as a nonlinear, almost threshold function of the detected signal current. With a digital counter reading the output of the bit error detector, the bit error rate for the sample of Figure 4-6 was found to be 4.1×10^{-3}

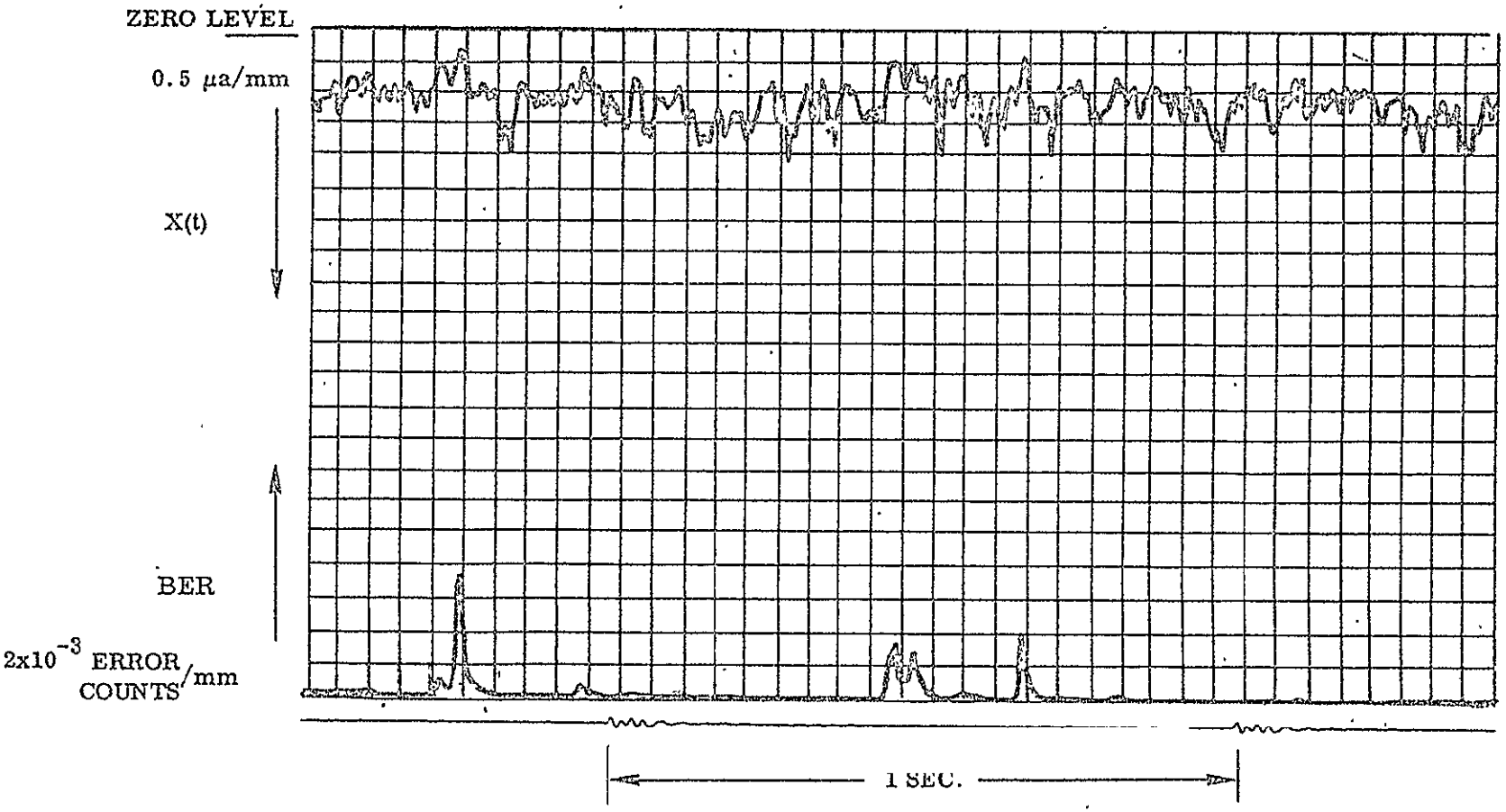

Figure 4-6. Sample Data Tape.

4.4 FIELD EVALUATION

The new 22 inch telescope discussed in section 2.2.1 was successful in allowing experimental control over the scintillation effects of atmospheric turbulence. The two photographs of Figure 4-7 show the irradiance distribution of the down-link laser beam across the full 22 inch aperture. These two photos were taken on different days with the same exposure — 1/1000 second. The differences in scintillation and the resultant variations in detected radiant powe are apparent.

It was pointed out in Section 3.2 that the system's bit error rate is a complex function of atmospheric scintillation amplitude r, the ratio of the measured standard deviation to the mean (of any linear function) of the detected signal radiation. The factor r is useful in predicting system performance and, as Figure 3-5 shows, is somewhat under the system designer's control in that scintillation amplitude is greatly affected by receiving aperture diameter. The curve of Figure 4-8 indicates the strong relationship between aperture diameter and a system's bit error rate. It should be noted that this curve considers the scintillation averaging effects of various aperture size, neglecting the greater radiation collecting ability of larger apertures. The bit error rate curve of Figure 4-8 would fall at a much greater slope if a constant detected power had not been maintained by attenuating the beam with neutral density filters as the aperture was increased.

Figure 4-9 shows the performance of the communications system in field tests under conditions of heavy turbulence. For comparison the theoretically predicted performance for $\rho = 0.35$ is represented as the solid curve on the right. Data runs with varying laser radiation intensities were recorded, and the results are shown as horizontal bars. The term r is an estimate of the parameter ρ, calculated from experiment data. Since r is a statistic of the non-stationary atmosphere, its value is constantly changing and the use of the

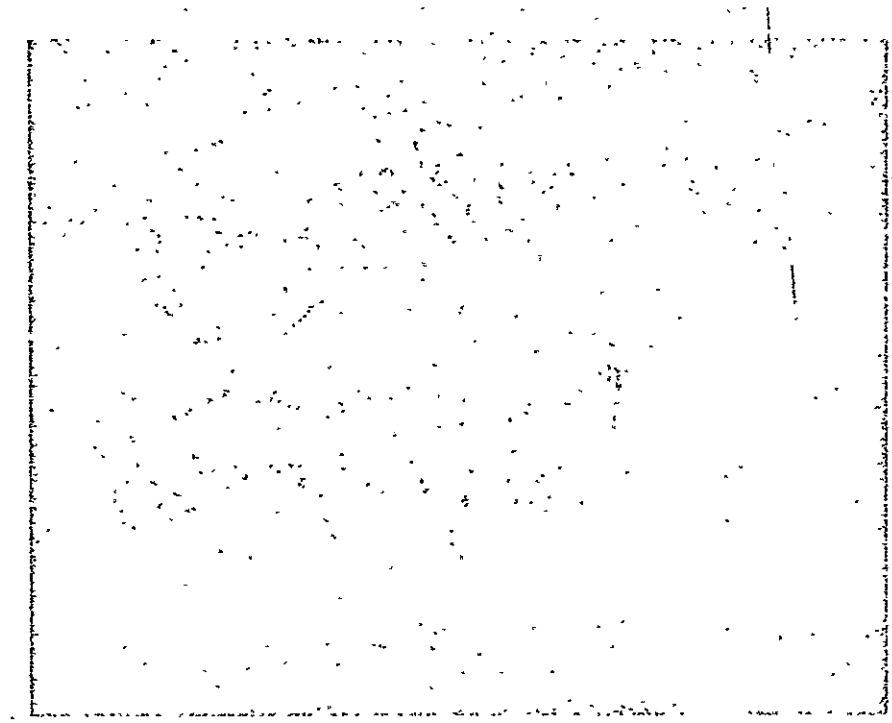

Figure 4-7a

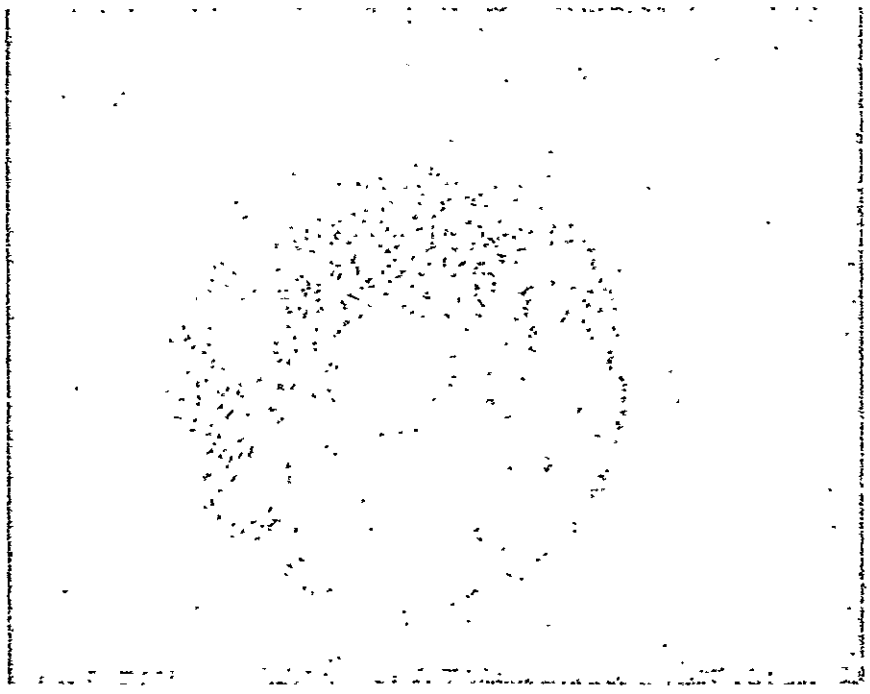

Figure 4-7b. Photographs of Laser Radiation Across the Aperture of the 22-Inch Telescope.

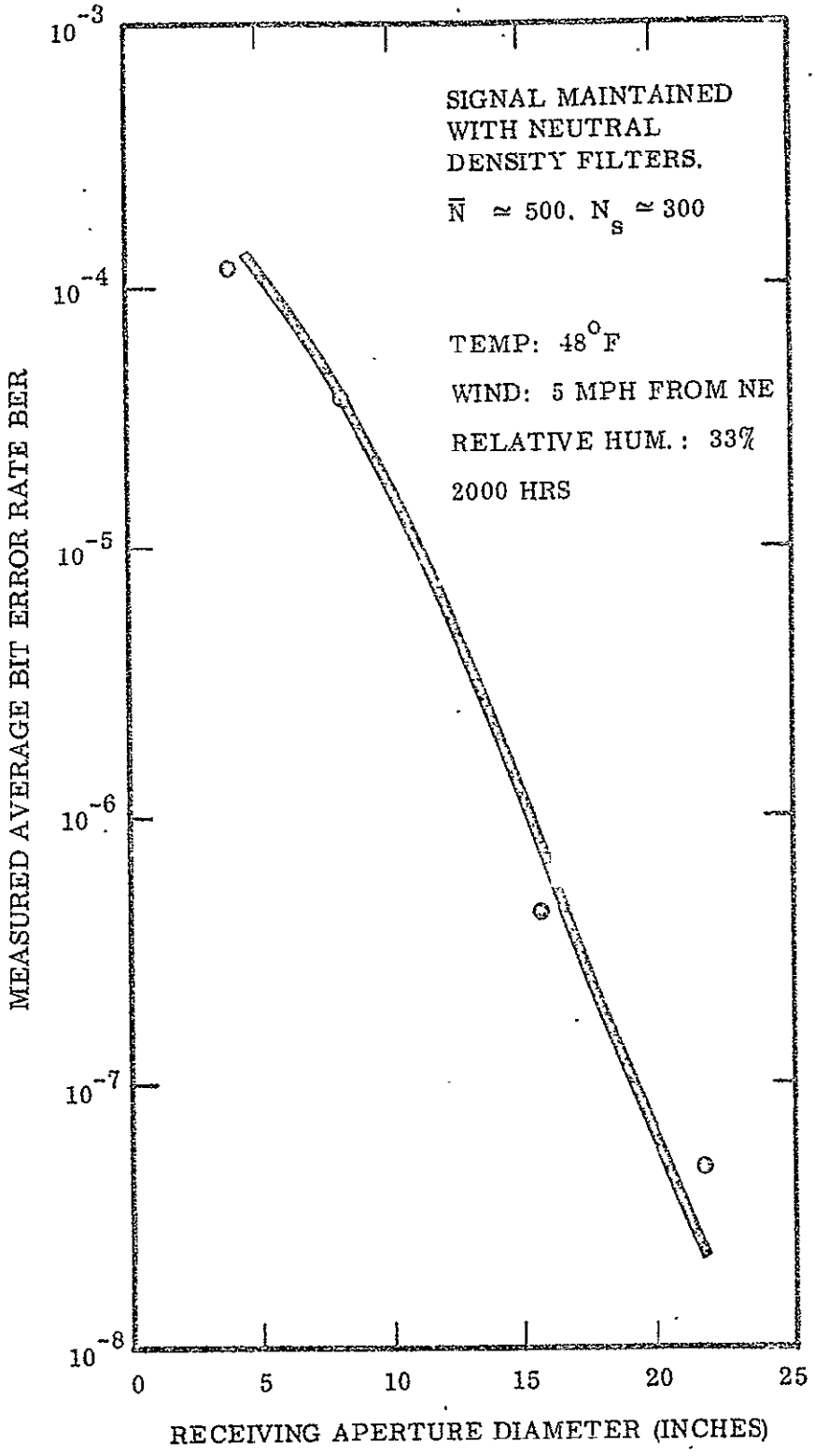

Figure 4-8. Bit Error Rate vs Receiving Aperture.

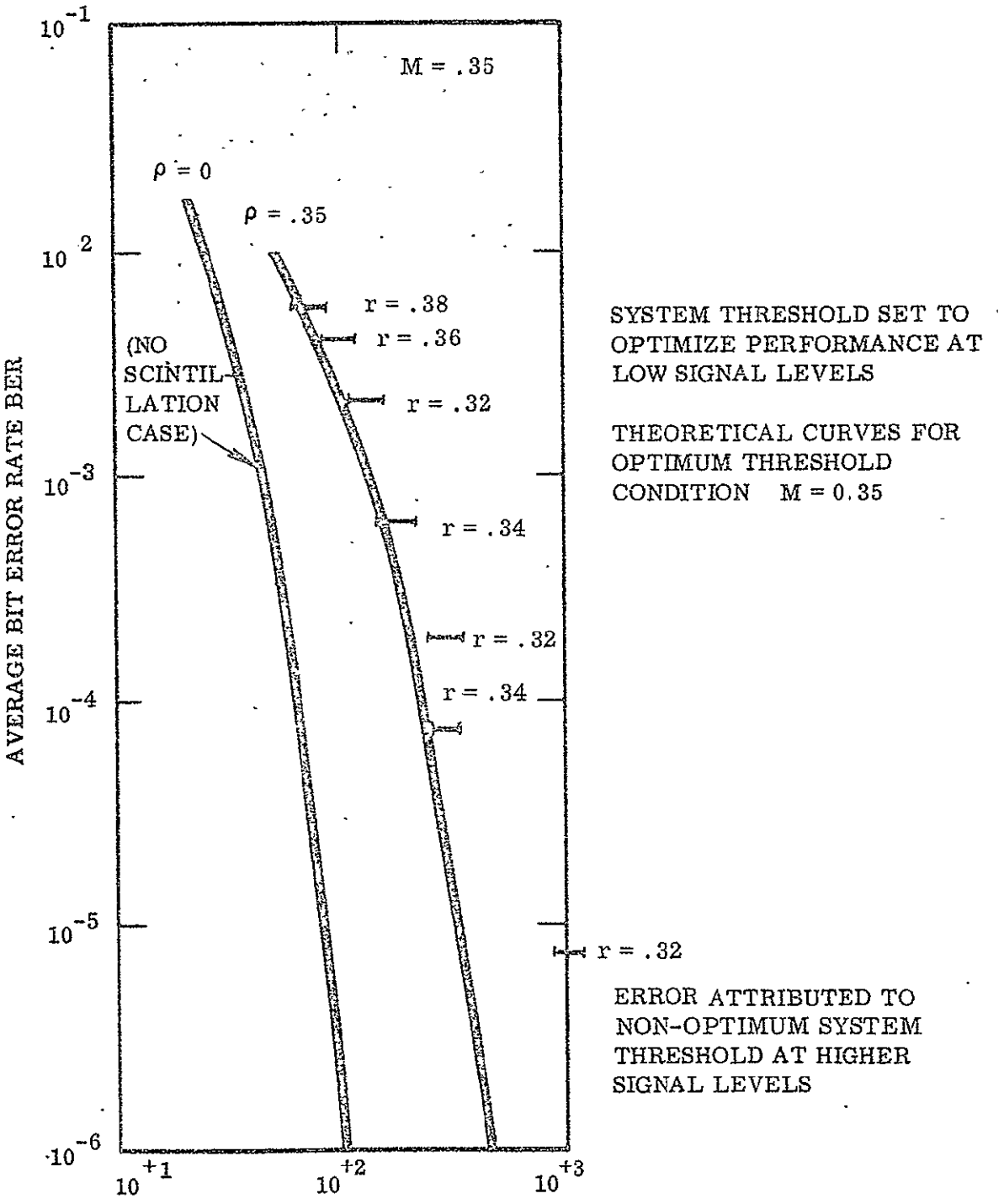

Figure 4-9. Comparison of Experimental Data With Log-Normal Atmospheric Model for Single Channel System.

bar interval is appropriate. The fit of theoretical predictions to the tested performance of the system is seen to be quite close.

The field performance of the binary system configuration is depicted in Figure 4-10 for two situations: $M = 0.35$, $r = 0.20$; and $M = 0.50$, $r = 0.38$. As indicated by curves in the figure, these two situations should have nearly equivalent performance. The fit of the experimental data to the theoretical model is seen to worsen for bit error rates less than 10^{-5}. One of the principal causes of this difference is likely to be slight differences between a real atmosphere and the log-normal model, which become apparent only at low bit error rates.

4.4 PROBLEM AREA

A rather persistent source of difficulty throughout this program has been the commercially purchased digital equipment. The alignment of the MARK V T-31A bit error detector has proven critical and difficult to achieve and to maintain. When the bit error output is terminated in the recommended 75 Ω load, the equipment generates ringing output pulses which our counter sees as 2 pulses. Furthermore, the equipment is quite critical about its acceptance of incoming pulsewidth. No analysis of this problem has been done but experience with the handwire error detector built at this facility has shown that more accurate pulse identification is possible.

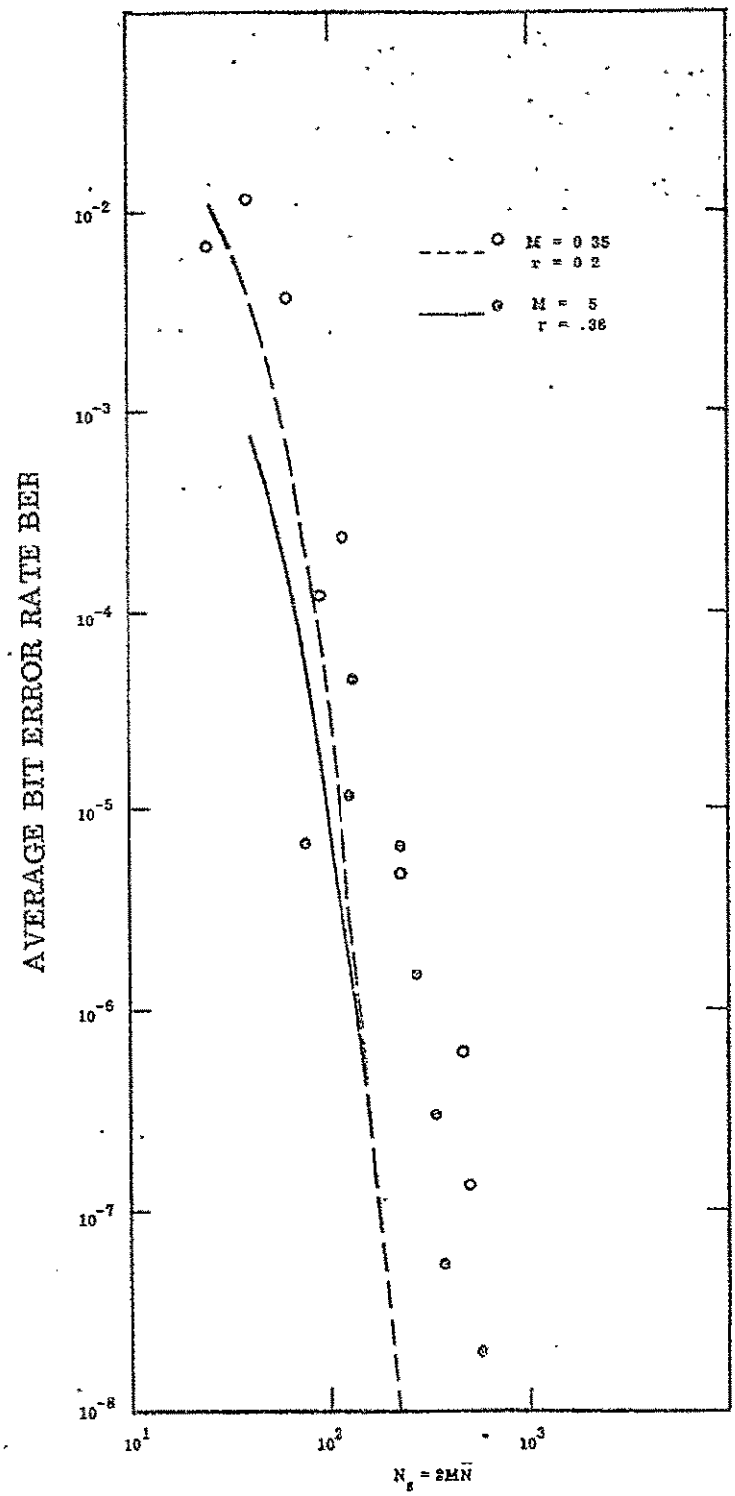

Figure 4-10. Comparison of Experimental Data with Mathematical Model for Binary Channel Systems.

REFERENCES

1. Ward, J.H., Interim Report "A Narrow Beam, Broad Bandwidth Optical Communication System, Contract NAS 8-20629, 6 October 1969.

2. Reference Data for Radio Engineers, Fourth Edition, International Telephone and Telegraph Corporation, NY, NY, page 409.

3. V.L. Tartarski, Wave Propagation in a Turbulent Medium, Translated by R.A. Silverman (McGraw-Hill Book Company, Inc., New York, 1961).

4. Cramer, Harold, Mathematical Methods of Statistics, Princeton University Press 1957.

5. D.L. Fried, "Aperture Averaging of Scintillation," J. Opt Soc. Am., Vol. 57, pp. 169-175, Feb. 1967.

LIST OF SYMBOLS AND ABBREVIATIONS

BER	Bit error rate (sec 3.1.2)
PSR	Pseudo-random (sec. 2.2.2)
D/A	Digital-to-analog conversion (sec. 2.1.3)
M	Modulation index (eq 3.1)
$\overline{A}, A_m, A_p, A_s$	Signal amplitudes (sec 3.1.1)
Var	Statistical variance (eq 3.2)
i_{p_c}, i_p, i_m	Photocurrents in electrons per second (sec 3.1.1)
Δt	Time interval in seconds, the inverse of the system bit transmission rate (eq 3.2)
N_t	Set number of photoelectrons per bit interval use as threshold decision value (sec 3.1.3)
$\overline{N}, N_p, N_m, N_s$	Number of photoelectrons per bit interval (defined from $\overline{N}$ as in sec 3.1.1)
k	Factor describing increase in current variance with a noisy amplification process (eq 3.2)
$\tilde{N}, \tilde{N}_p, \tilde{N}_m$	Random variables describing numbers of photoelectrons in an ideal system (sec 3.1.3)
P, Q	Tabulated probability error functions (eq 3.7)
a	Random variable describing noise multiplicative with signal (eq 3.17)